Achieving Exceptional Volumetric Desalination Capacity Using Compact MoS_2 Nanolaminates

Ting Ying[1]†, Yu Xiong[1]†, Huarong Peng[1]†, Ruijie Yang[1], Liang Mei[1], Zhen Zhang[1], Weikang Zheng[1], Ruixin Yan[1], Yue Zhang[1], Honglu Hu[1], Chen Ma[2], Ye Chen[2], Xingtao Xu[3], Juan Yang[4], Damien Voiry[5], Chuyang Y. Tang[6], Jun Fan[1], Zhiyuan Zeng[1,7*]

[1]Department of Materials Science and Engineering, and State Key Laboratory of Marine Pollution, City University of Hong Kong, 83 Tat Chee Avenue, Kowloon, Hong Kong S.A.R. 999077, P. R. China.

[2]Department of Chemistry, The Chinese University of Hong Kong, Hong Kong S.A.R. 999077, China.

[3]Marine Science and Technology College, Zhejiang Ocean University, Zhoushan, Zhejiang 316022, China.

[4]School of Chemical Engineering and Technology, Xi'an Jiaotong University, Xi'an, 710049 China.

[5]Institut Européen des Membranes, IEM, UMR 5635, Université Montpellier, ENSCM, CNRS, Montpellier 34000, France.

[6]Department of Civil Engineering, The University of Hong Kong, Hong Kong S.A.R. 999077, China.

[7]Shenzhen Research Institute, City University of Hong Kong, Shenzhen 518057, P. R. China.

†These authors contributed equally to this work.

*Corresponding authors: zhiyzeng@cityu.edu.hk (Z. Y. Zeng)

Abstract

Capacitive deionization (CDI) has emerged as a promising technology for freshwater recovery from low-salinity brackish water. It is still inapplicable in specific scenarios (*e.g.*, households, islands, or offshore platforms) due to too low volumetric adsorption capacities. In this study, we report a high-density semi-metallic molybdenum disulfide (1T′-MoS_2) electrode with compact architecture obtained by restacking of exfoliated nanosheets, which achieved high capacitance up to ~277.5 F cm^{-3} under an ultrahigh scan rate of 1000 mV s^{-1} with a lower charge-transfer resistance and nearly ten-fold higher electrochemical active surface area than the 2H-MoS_2 electrode. Furthermore, 1T′-MoS_2 electrode demonstrates exceptional volumetric desalination capacity of 65.1 mg_{NaCl} cm^{-3} in CDI experiments. *Ex-situ* X-ray diffraction (XRD) reveal that the cation storage mechanism with the dynamic expansion of 1T′-MoS_2 interlayer to accommodate cations such as Na^+, K^+, Ca^{2+}, and Mg^{2+}, which in turn enhances the capacity. Theoretical analysis unveils that 1T′ phase is thermodynamically preferable over 2H phase, the ion hydration and channel confinement also play critical role in enhancing ion adsorption. Overall, this work provides a new method to design compact two-dimensional layered nanolaminates with high volumetric performance for CDI desalination.

Introduction

Freshwater scarcity is a global challenge, and the additional pollution of freshwater by industrial or agricultural activities poses a significant threat to human health[1]. To guarantee adequate freshwater supply, desalination has emerged as a promising solution, utilizing abundant seawater and brackish water resources. Conventional desalination techniques, such as reverse osmosis and membrane distillation, are widely employed for treating seawater and brackish water, but they are energy-intensive[2-4]. Alternatively, capacitive deionization (CDI) offers an energy-efficient and low-carbon footprint approach for removing ions from low-salinity brackish water (concentration < 1000 mg L^{-1})[5-11]. Besides, CDI has been utilized to remove heavy metal ions from industrial wastewater and harmful ions in groundwater[12-13].

The principle of CDI is the electrostatic or electrochemical adsorption of ions from aqueous solution to electrodes, which is similar to electrical double-layer capacitors (EDLC)[14]. Thus, the selection of high performance and space-applicable electrode materials is crucial for the industrialization of CDI technique[15-16]. In decades, carbon-based materials[17-19], including graphene-based material[20-21], porous carbon[6] as well as derived carbon[22] have been extensively investigated owing to their desirable porosity for high ions absorbed surface area. These low density carbon-based electrodes (0.4 ~ 0.7 g cm^{-3})[23], delivery a high gravimetric desalination performance but compromising their volumetric one. That makes a challenge to practically employ the CDI technique in certain specific scenarios (*e.g.*, households, islands, or offshore platforms) requiring efficient utilization of space[24]. In addition, despite the characteristic microporosity of carbon-based materials contributing to large specific surface area, their closed micropores or narrow apertures hamper ion diffusion and thereby slowing down desalination rates[25-26]. Consequently, achieving compact electrodes with both satisfactory gravimetric and volumetric desalination performance is a challenging yet essential task[14, 24].

Two-dimensional (2D) materials, e.g., transition metal carbides (MXenes)[27-28] and transition metal dichalcogenide (TMDs)[29-30], possess tunable nanochannels, enabling promising electrochemical adsorption of ions and thereby benefiting the desalination performance[31]. Nonetheless, owing to hydrophilic functional groups attaching to basal plane[25, 32], MXenes tend to swell in aqueous solution, leading to easily structural

disintegration, undesirable CDI performance and poor recyclability[17]. TMDs, especially MoS_2, are more chemically stable than reported MXenes in seawater and brackish water, making it an optimal candidate for CDI electrode materials[33-34]. MoS_2 exists in various polymorphs, including 2H, 1T and 1T′ phases, distinguished by different intralayer stacking order[35-37]. These different phases have distinct physical and chemical properties that impact ions electro-sorption performance. Among these polymorphs, the semi-metallic 1T′ phase MoS_2 is the thermodynamically preferred and has shown promise in electrochemical energy storage[29, 38]. However, the potential of the 1T′-MoS_2 in CDI system has been underestimated.

In this study, we demonstrate 1T′-MoS_2 nanolaminates with stable nanochannels and compact architecture as superior CDI electrode materials, showing an ideal EDLC behavior and thus achieving high volumetric desalination performance. Our work reveals the nature of ions storage mechanism lies in the dynamically stable nanochannels of 2D layered materials experimentally and theoretically. Specifically, *Ex-situ* XRD results demonstrate the adsorption and storage of cations (*e.g.*, Na^+, K^+, Ca^{2+}, and Mg^{2+}) within the 1T′-MoS_2 interlayer leads to the dynamic expansion of nanochannels, which in turn improve the desalination capacity. Theoretical calculations indicate that the phase structure factor governs cations adsorption behavior whereas ion hydration and channel confinement effects further enhance the performance. These findings rationalize the design of compact 1T′-MoS_2 nanolaminates for CDI electrodes and guide the development of other 2D layered materials with high desalination performance.

Results and discussion

Fabrication and characterizations

The 1T′-MoS_2 nanosheet aqueous suspension was obtained using our previously reported protocol[39-41], *i.e.*, electrochemical lithium intercalation-based exfoliation from bulk 2H-MoS_2 powder (see Methods) (see **Figure S1** for the scanning electron microscope [SEM] image and XRD pattern of the original MoS_2 powder). The 2H-MoS_2 nanosheet aqueous suspension, as a control, was also prepared via a simple solvent exfoliation method[42]. Subsequently, 1T′-MoS_2 and 2H-MoS_2 electrode were further fabricated by restacking the exfoliated nanosheets onto a flexible current collector via vacuum filtration and dehydration (**Figure 1a**). Note that the zeta potential

value of 1T′-MoS_2 nanosheets is negative (-53.2 mV, **Figure S2**), indicating the presence of negative charges.

Transmission electron microscopy (TEM) image (**Figure 1b**) shows the flake-like morphology of the exfoliated 1T′-MoS_2 nanosheets. The selected area electron diffraction (SAED) pattern exhibits a typical diffraction pattern of hexagonal symmetry (inset of **Figure 1b**). Atomic force microscopy (AFM) analysis (**Figure S3**) confirms the ultra-thin attribute of the exfoliated 1T′-MoS_2 nanosheets with thickness ranging from 1.1 to 1.8 nm. Scanning transmission electron microscopy (STEM) images (**Figure 1c** and **Figure S4-S6**) display a distinctive Mo atomic structures of zigzag chains with shortest Mo-Mo distance of 2.79 Å (**Figure S5**) of the lithium intercalation-based exfoliated MoS_2 nanosheets, suggesting their distorted octahedral (1T′) phase[35] (**Figure 1d**), which was further confirmed by the corresponding fast Fourier transform (FFT) pattern (inset of **Figure 1c**).

The prepared 1T′-MoS_2 electrode exhibits excellent flexibility (**Figure 1f**). Cross-sectional SEM image (**Figure 1g**) reveals the typical lamellar and compact architecture of 1T′-MoS_2 electrode with a thickness of 1000 nm. Varying thickness (i.e., 300 nm, 2000 nm, 3000 nm, and 4300 nm) of 1T′-MoS_2 electrodes can be prepared by adjusting the volume of filtrated solution (**Figure S7**). The surface of the prepared electrode is notably flat, as confirmed by the average surface roughness value of 37 nm (**Figure S8**). High-resolution TEM (HR-TEM) image demonstrates the interlayer spacing of 0.62 nm from horizontal MoS_2 nanolaminates (**Figure 1h**), which is close to the spacing observed in bulk MoS_2. Characteristic peaks of 2H-MoS_2 dispersion located at 409, 478, 615 and 673 nm, can be clearly observed in the UV-Vis absorption spectra as denoted by the dashed lines (**Figure S9**). Raman peaks of the 2H-MoS_2 electrode (**Figure 2a**), located at 377.4 and 402.7 cm^{-1} are two characteristic modes[41], corresponding to E_{2g} (in-plane vibration) and A_{1g} (out-of-plane vibration). Conversely, the 1T′-MoS_2 electrode exhibits additional modes such as J_1 (148.3 cm^{-1}), J_2 (221.2 cm^{-1}), J_3 (326.1 cm^{-1}), and E_{1g} (286.1 cm^{-1}), along with the absence of E_{2g} modes[43]. In the X-ray diffraction (XRD) patterns (**Figure 2b**), the peak of the (002) plane for the dehydrated 1T′-MoS_2 electrode is located at approximately 14°, validating the quasi-perfect restacking of the pristine nanosheets, resembling that of bulk MoS_2[29, 44]. The average (002) spacing of the dehydrated 1T′-MoS_2 electrode is 0.63 nm, consistent with HR-

TEM results (**Figure 1h**). Due to the hydrophilic nature of 1T′-MoS_2 (**Figure S10**), the peak of hydrated 1T′-MoS_2 electrode shifted to a lower angle of 8.5°, corresponding to spacing of 1.0 nm (**Figure 2b**). In contrast, the (002) plane of 2H-MoS_2 electrode closely aligns with the position of bulk MoS_2 powder (14.3°, **Figure S1**). X-ray photoelectron spectroscopy (XPS) was employed to examine the chemical states of the two electrodes from the Mo 3d (**Figure 2c** and **2d**) and S 2p (**Figure 2e** and **2f**) regions. For the 2H-MoS_2 electrode, **Figure 2c** presents deconvolution of the Mo 3d regions (227 - 234 eV) of two distinct peaks, indicating the exclusive presence of the 2H phase. This is further confirmed by the presence of only two characteristic peaks in the S 2p spectrum (160 - 165 eV) (**Figure 2e**). In contrast, 1T′-MoS_2 electrode (**Figure 2d**) exhibits characteristic peaks of the 1T′ phase, which shifted to lower values by approximately 0.8 eV compared with the 2H phase[43]. Based on the XPS data from the Mo 3d region (**Table S1**), the percentage of 1T′ phase can reach up to 73%. **Figure 2f** demonstrates that the exfoliated MoS_2 nanosheets display two doublets in the S 2p region, consistent with the presence of both 1T′ and 2H phases in exfoliated MoS_2. According to characterizations above, we finally confirmed the 1T′-MoS_2 nanolaminates with stable nanochannels and compact architecture were successfully fabricated.

Electrochemical properties

To differentiate the effect of polymorphs on CDI desalination performance, the electrochemical properties of the 2H and 1T′-MoS_2 electrodes, were evaluated by cyclic voltammetry (CV) using a conventional three-electrode set-up at room temperature in a 1 M KCl electrolyte, where the Ag/AgCl electrode and Pt plate served as reference and counter electrodes, respectively. The near-rectangular and symmetric shape of 1T′-MoS_2 electrode indicates typical EDLC behavior, achieving a capacitance of 95 F g^{-1} at 50 mV s^{-1}, in contrast to the less favorable shape observed for 2H-MoS_2 electrode with 35 F g^{-1} (**Figure 3a**). As scan rates increase from 10 to 1000 mV s^{-1}, the well preserved EDLC behavior of the 1T′-MoS_2 electrode demonstrates its robust performance under ultrahigh charge and discharge rate (**Figure 3b**) while the capacitance of 2H-MoS_2 electrode deteriorates at 100 mV s^{-1} (**Figure S11**). Specifically, the 1T′-MoS_2 electrode delivers a capacitance of 101 F g^{-1} (373 F cm^{-3}) at 20 mV s^{-1} and slightly decreases with increased scan rates from 50, 80, 100, 200, 500, 800 to 1000 mV s^{-1}, but remains at 75 F g^{-1} (277.5 F cm^{-3}) even under ultrahigh scan rate of 1000

mV s^{-1}, highlighting its excellent rate performance (**Figure 3c**). **Figure 3d** presents the galvanostatic data collected at different current densities (1, 2, 5, 10 and 20 A g^{-1}) with corresponding charging and discharging time ranging from 107, 37, 11, 6, 2 seconds respectively. The triangular and symmetric shapes also support the EDLC effect of 1T′-MoS_2 electrode. The electrochemical impedance spectroscopy (EIS) results provide a powerful platform to analyze the electron transfer properties. Notably, the charge-transfer resistance (R_{ct}) between the electrode and interface is closely related to the diameter of the quasi-semicircle. As shown in **Figure 3e**, the 1T′-MoS_2 electrode exhibits a lower R_{ct} of 2.5 Ω cm^2 compared with the 7 Ω cm^2 for 2H-MoS_2 electrode. The analysis of the electrochemical active surface area (ECSA) (**Figure 3f** and **Figure S12**) reveals that the ECSA value of 1T′-MoS_2 (2725 cm^2_{ECSA}) is nearly ten-fold greater than that of 2H-MoS_2 (300 cm^2_{ECSA}), demonstrating the superiority of 1T′-MoS_2 in electrochemical active surface area.

Capacitive desalination performances

To further investigate the impact of polymorphs on electro-sorption of ions, we conducted evaluations of the CDI desalination performance using NaCl solution (low salinity, 500 mg L^{-1}) in constant-voltage single-batch measurements. **Figure 4a** presents a schematic illustration of the CDI working mechanism. Specifically, two symmetric electrodes were immersed in aqueous solutions with a conductivity meter inserted in the middle of the cell to monitor conductivity (**Figure S13** and **Figure S14**). The salt adsorption capacity measured in gravimetric adsorption capacity (GAC, Γ_g, mg_{NaCl} g^{-1}) is an important indicator reflecting the maximum salt adsorption capability. As shown in **Figure 4b**, when a bias voltage of 0.5 V was applied across the two electrodes, the GAC of the 1T′-MoS_2 electrode increases to 13 mg_{NaCl} g^{-1} within the first 200 seconds and gradually approaches a steady capacity of 17.6 mg_{NaCl} g^{-1} in the following 1000 seconds. In contrast, the GAC of the 2H-MoS_2 electrode quickly reaches a plateau of 5 mg_{NaCl} g^{-1} within the first 100 seconds. The increased GAC curves of the electrodes agreed well with the current density profiles (**Figure S15**)[6]. **Figure 4c** shows the average salt adsorption rate (ASAR) in the form of Kim-Yoon Ragone diagram[45]. The ASAR of 2H-MoS_2 electrode quickly drop below 1 mg_{NaCl} g^{-1} min^{-1} when GAC exceeds 6 mg_{NaCl} g^{-1} while 1T′-MoS_2 electrode can maintain the ASAR over 1 mg_{NaCl} g^{-1} min^{-1} until the GAC approaches 16 mg_{NaCl} g^{-1}, further demonstrating the rapid desalination performance of our 1T′-MoS_2 electrode.

We also investigated the effect of electrode thickness on the adsorption capacity with different initial saline concentrations. As shown in **Figure 4d**, all the GAC of electrodes with different thicknesses (300, 1000, 2000, 3000, and 4300 nm) follow the Langmuir adsorption isotherm representing the relationship between the quantity of adsorbed salt and the NaCl initial concentration (dashed lines). We found that the thickness of the electrodes influenced the adsorbed quantities. For instance, when the initial NaCl concentration is 500 mg L^{-1}, the NaCl adsorption quantity for electrodes with thicknesses of 300, 1000, 2000 nm is 16.9, 17.6, 13.2 mg_{NaCl} g^{-1}, respectively. Obviously, too thick nanochannels may introduce resistance in cation transport, thereby reducing the overall adsorption capacity. When increasing the NaCl initial concentration from 1000 to 2000 mg L^{-1}, the NaCl adsorption reaches saturation, and the GAC of 300, 1000, 2000 nm-thickness electrode remains at 17.1, 17.6, 15.4 mg_{NaCl} g^{-1} respectively, indicating the capacity is related with the thickness. **Figure S16** shows the XPS depth profile of the Na element after CDI measurements, exhibiting uniformly distributed adsorbed Na^+ within the MoS_2 layers. The depth ranges from 30 to 90 nm, corresponding to c.a. 48 to 145 layers of MoS_2.

For long-term stability assessment, the 1T′-MoS_2 electrode was subjected to 25 charge-discharge repeats with recycled CDI operation, rinsing, and re-hydration. After 40 cycles, the average GAC of 1T′-MoS_2 remained at approximately 14.61 mg_{NaCl} g^{-1} (83%), indicating that CDI electrodes exhibited no substantial loss of desalination capacity after repeated charge-discharge cycles (**Figure 4e**). Post characterization also showed structural integrity after the CDI experiment, confirming the physical stability of our 1T′-MoS_2 electrode (**Figure S17** and **Figure S18**). Furthermore, we evaluated the versatile performance of the 1T′-MoS_2 electrode in different saline solutions. As depicted in **Figure 4f**, the gravimetric desalination capacity for K^+ was the highest (22.0 mg g^{-1}), followed by Na^+ (17.6 mg g^{-1}), Ca^{2+} (15.1 mg g^{-1}), and Mg^{2+} (12.6 mg g^{-1}). The molar desalination capacity of Na^+ (0.301 mmol g^{-1}) and K^+ (0.295 mmol g^{-1}) was similar, while Ca^{2+} (0.136 mmol g^{-1}) and Mg^{2+} (0.134 mmol g^{-1}) were approximately half as much. This result suggests that the quantity of carrying charges (e.g., K^+/Na^+ with one charge and Ca^{2+}/Mg^{2+} with two charges) may determine the maximum electro-adsorption capacity. Based on the results, the 1T′-MoS_2 electrode was versatile and capable of removing common cations, i.e., K^+, Na^+, Mg^{2+}, and Ca^{2+} from low-salinity brackish water.

The calculation of volumetric adsorption capacity (VAC, Γ_V, mg_{NaCl} cm^{-3}), is analogous to the volumetric capacitance (C_v, F cm^{-3}) which is determined by the product of gravimetric capacitance (C_g, F g^{-1}) and the density of electrodes (ρ, g cm^{-3})[46]. Therefore, the volumetric desalination capacity of our compact 1T′-MoS_2 electrode can be expressed as[29],

$$\Gamma_V = \Gamma_g \times \rho \quad (1)$$

Here, the density of the hydrated electrode (ρ) was measured to be approximately 3.7 g cm^{-3} owing to the densely compact architecture, which is lower than that of reported bulk MoS_2 powder[44] but higher than carbon-based materials ones[23]. To provide an overview of the performance compared with state-of-the-art electrodes, we summarized the VAC and GAC of 1T′-MoS_2 electrode in **Figure 4g**, with data from previous literature on carbon-based and 2D-based materials (**Table S2**)[47]. The red star representing our EDLC-type 1T′-MoS_2 electrode demonstrates superior VAC performance (65.1 mg_{NaCl} cm^{-3}), and its GAC performance (17.6 mg_{NaCl} g^{-1}) is excellent when compared with state-of-the-art materials. Notably, our EDLC-type 1T′-MoS_2 electrodes exhibited improved VAC performance based on the utilization of horizontal nanochannels of compact architecture.

Cation storage mechanism

Ex situ XRD measurements were performed on CDI electrodes intercalated with different electrolytes including deionized water and 0.5 M saline solutions (NaCl, KCl, $CaCl_2$ and $MgCl_2$) to investigate the cation storage mechanism in 1T′-MoS_2 electrodes (**Figure 4h**). As intercalation proceeds, the intensity of the (002) peak at 14.1° from restacked 1T′-MoS_2 decreases slightly, and the intensity of new peak appears at lower angle, indicating that interlayer expansion between consecutive S-Mo-S layers caused by intercalation of cations or water molecules. Notably, the extent of interlayer spacing expansion strongly depends on the types of intercalants. Expansions of the spacing between consecutive S-Mo-S layers are 4.0 Å, 5.8 Å, 5.2 Å, 6.1 Å, 6.3 Å for pure water, Na^+, K^+, Ca^{2+} and Mg^{2+}, respectively. This finding is also related to the fact that hydrated diameter of K^+ (6.62 Å) is smaller than that of Na^+ (7.16 Å), Ca^{2+} (8.24 Å) and Mg^{2+} (8.56 Å). The dynamic expansion of the interlayer spacings of the 1T′-MoS_2 suggests that the electrodes are capable of accommodating cations dynamically[38], which in turn, is beneficial to the enhancement of desalination capacity.

To further elucidate the cation storage mechanism during CDI process, we distinguished the crucial roles of structure factor, ion hydration, and confinement effects in desalination performance using density functional theory (DFT) calculations and ab initio Molecular Dynamics (AIMD) simulations. The adsorption energy (E_{ad}) for a single K^+ on different initial sites of the 1T′ and 2H-MoS_2 surfaces were first calculated and summarized (**Figure S19**). We selected the configuration with the most favorable adsorption site (most negative values of E_{ad}) and presented the structures, *i.e.*, Mo_1 site on 1T′-MoS_2 (Mo_1-1T′), Mo site on 2H-MoS_2 (Mo-2H) and respective 2D channels were constructed (see the top and side view of atomic structures in **Figure 5a** and **Figure S20**). As shown in **Figure 5b**, the E_{ad} of Mo_1-1T′ (-2.38 eV) is significantly lower than that of Mo-2H (-0.73 eV) in the vacuum state, suggesting the 1T′ phase exhibits enhanced adsorption capabilities against the 2H phase. This is because the 1T′ phase shows a higher degree of asymmetry, resulting in an active surface with increased adsorption sites, and thus a more conducive adsorption structure compared with the 2H phase. Upon the introduction of a K^+ within the MoS_2 channel, the E_{ad} for Mo_1-1T′ (-2.79 eV) and Mo-2H (-1.26 eV) decrease slightly, indicating that channel confinement effect can facilitate the ion adsorption. Surprisingly, when accounting for the solvent effect, the E_{ad} of K^+ nearly doubles (-4.47 eV for 1T′-MoS_2 while -2.93 eV for 2H-MoS_2), indicating that the solvation enhanced the interaction between the K^+ and the MoS_2 channel. These results highlight the important factors of both confinement and hydration effects contributing to exceptional adsorption performance. Similar trends were found for other adsorption sites as the E_{ad} of 2H-MoS_2 were smaller than that of 1T′-MoS_2 at all possible adsorption sites (See **Table S3**).

To investigate the diffusion behavior of ions in the channel of 1T′ and 2H-MoS_2, we analyzed the diffusion energy barriers based on the climbing image nudged elastic band (CI-NEB) method. **Figure 5c** displays a higher diffusion barrier for the 1T′-MoS_2 channel (0.079 eV) compared with 2H-MoS_2 channel (0.048 eV), suggesting a more challenging migration path in the 1T′ channel. While easy migration may facilitate ion transport, it may hamper effective ion adsorption. For the study of ions hydration effect, the AIMD simulations were performed to analyze the hydration structure of solvated ions in the channel of MoS_2 with different phases (**Figure S21** and **Supplementary Video 1** for 1T′-MoS_2, **Figure S22** and **Supplementary Video 2** for 2H-MoS_2). We note that coordination number (CN) distribution of water molecules varies from the 1T′

to 2H phase. For a K^+ in the 1T′ channel, the majority of CN is predominantly 5 (91.77%), while the CN of the 2H phase is 6 (55.81%) (**Figure 5d**). The decreased CN of the hydration shell resulted in partial exposure of the K^+ core, allowing direct contact with the 1T′-MoS_2 layer and thus enhancing the interaction between the metal ion and the layered materials[48]. Next, the Bader charge density analysis suggests that more charge transfers from K^+ to the 1T′ channel (0.82 |e|) than the 1T′ surface (0.80 |e|), as demonstrated in **Figure 5e** and **Figure S23**. Such charge transfer indicates the increased ion-MoS_2 interaction when ions exist in the limited nanochannels. Overall, our theoretical calculations demonstrate that the 1T′-MoS_2 structure governs K^+ adsorption behavior by increasing the interaction of K ions to their adsorption sites in the S-Mo-S channel, thereby providing a superior desalination performance in CDI applications.

Conclusion

In summary, our study has demonstrated that the compact 1T′-MoS_2 electrode, devoid of binders, exhibits ideal EDLC behavior at 1000 mV s^{-1} and displays high volumetric desalination performance (65.1 mg_{NaCl} cm^{-3}) in CDI configurations. This exceptional performance can be attributed to the metastable 1T′ phase structure of MoS_2, compact laminated architecture featuring intrinsic nanochannels, bringing about its unique characteristics of low charge-transfer resistance and high electrochemical active surface area to accommodate various cations. The experimental analysis and theoretical calculations have revealed that compared with 2H phase, cations prefer adsorbed on the Mo sites of 1T′-MoS_2 and in the channels of the 1T′ phase. Moreover, ion hydration and channel confinement effects help to enhance ion adsorption performance. Following these results, we believe that our EDLC-type 1T′-MoS_2 electrode can be favorable state-of-the-art nanolaminated materials for integration into miniaturized CDI desalination system.

Methods

Exfoliation of MoS_2 bulk powder. The MoS_2 nanosheets obtained by electrochemical lithium exfoliation-based intercalation are on ground of previous reported protocol[35-37]. Typically, the slurry containing MoS_2 powder, carbon black, and PVDF (8:1:1) mixed with NMP was fabricated into an electrode plate. The plate acted as a cathode was assembled into a testing coin cell and then discharged to perform the lithium intercalation. After that, the lithium-intercalated cathode (Li_xMoS_2) was separated from

the dissembled cell when the discharging process finished. Finally, the MoS_2 nanosheets were obtained *via* sonication of the electrodes in DI water for one hour, during which the generated gas (H_2) bubbles accelerated the exfoliation of the bulk MoS_2. The centrifugation and re-dispersion process (repeated at least three times) is indispensable to remove the multiple layers of MoS_2 nanosheets. Thus, single layer of 1T′-MoS_2 nanosheets were successfully synthesized.

Preparation of MoS_2 electrodes. The 1T′-MoS_2 electrode were fabricated through vacuum filtration reported previously[34]. Briefly, porous polymeric supports were sputtering coated with Au thin layer first. Of note, polymeric supports are typically made of nylon or PVDF with 220 nm pore sizes. Then, the suspension of exfoliated 1T′-MoS_2 nanosheets was filtered over flexible, conductive polymeric supports. The density of the 1T′-MoS_2 hydrated electrodes were measured to be ~ 3.7 g cm^{-3}. The 2H-MoS_2 electrode was fabricated by filtration suspension of solvent exfoliation of bulk materials as previously reported[42].

Electrochemical measurements and CDI performance. The electrochemical performance was measured in a three-electrode system at room temperature with variation less than 0.3 °C. A Pt plate, an electrode (Ag/AgCl), 1 M KCl aqueous solution were used as the counter electrode, the reference electrode, and the electrolyte, respectively. Cyclic voltammetry (CV), galvanostatic charge-discharge (GCD), electrochemical impedance spectroscopy (EIS) and cycling stability studies were carried out on an Ivium potentiostat system. CV scans were conducted at scan rates ranging from 10 to 1,000 mV s^{-1}. Galvanostatic cycling scans were performed at current densities ranging from 1 to 20 A g^{-1}. The EIS was performed with frequencies ranging from 100 kHz to 0.01 Hz and a sinusoidal voltage of 5 mV. The batch-mode CDI experiment was carried out in a custom-made cell filled with 20 mL saline solution at room temperature with the variation less than 0.3 °C. The symmetrical electrode system was assembled using as-prepared electrodes, then immersed in the saline solution to serve as working and counter electrodes. A conductivity meter (SevenMulti, METTLER TOLEDO) was used to monitor the conductivity of the NaCl solution in real time curves (**Figure S13**). The conductivity of NaCl solution is linear relative to the concentration, as depicted in calibration curves (**Figure S14**). The desalination potential was set at a relatively low constant voltage (0.5 V) to avoid hydrogen

evolution reaction. Before measurements, the two electrodes were submerged in the solution without an external bias to minimize the effects of initial physisorption.

Computational method. All calculations were carried out by the Vienna ab initio simulation package (VASP) based on density functional theory (DFT)[49-51]. The generalized gradient approximation (GGA) of the Perdew-Burke-Ernzerhof (PBE) exchange correlation functional was used to describe the exchange-correlation interactions[52-54]. The plane-wave cutoff energy was set to 500 eV. The convergence standard for the total energy and ionic force were set to 10^{-5} eV and 0.02 eV $Å^{-1}$, respectively. The DFT-D3 method was employed to consider the influence of van der Waals (vdWs) interaction. To study the influence of water on ion adsorption on the MoS_2 channel, the implicit solvation (VASPsol) correction was applied[55-56]. The dielectric constant of water was set to $\varepsilon_b = 78.4$. In addition, the ab initio molecular dynamics (AIMD) simulations were performed to understand the transport properties and hydration structure of solvated ions in the MoS_2 channel. The simulation parameters were set to 300 K in a total of 30 ps with the time step of 1 fs.

Acknowledgements

Z.Y. Zeng thanks the Young Collaborative Research Grant [Project No. C1003-23Y] and General Research Fund (GRF) [Project No. CityU11308923] support from the Research Grants Council of the Hong Kong Special Administrative Region, China, the Basic Research Project [No. JCYJ20210324134012034] from Shenzhen Science and Technology Innovation Committee in Shenzhen, China, the Applied Research Grant of City University of Hong Kong (project no of 9667247) and Chow Sang Sang Group Research Fund of City University of Hong Kong (project no of 9229123). Z.Y. Zeng also thanks the funding supported by the Seed Collaborative Research Fund Scheme of State Key Laboratory of Marine Pollution which receives regular research funding from Innovation and Technology Commission (ITC) of the Hong Kong SAR Government. However, any opinions, findings, conclusions or recommendations expressed in this publication do not reflect the views of the Hong Kong SAR Government or the ITC. J. Fan thanks the Hong Kong Research Grant Council Collaborative Research Fund [No. C1002-21G]. This research made use of the computing resources of the X-GPU cluster supported by the Hong Kong Research Grant Council Collaborative Research Fund [No. C6021-19EF].

Author information

Z.Y.Z. conceived the research and guided the project. T.Y. and H.P. prepared the electrode samples and completed most of the experiments and characterizations. L.M., W.Z., R. Y., Y.Z., and H.H. helped with XPS, XRD analysis. Y.X. and J.F. carried out theoretical calculations and analysis. Z.Z. performed STEM characterizations and analyzed the data. C.M., and Y.C. helped with the TEM characterizations. X.X., J. Y., D.V., and C. T. provides helpful discussion into the experiment and the manuscript. T.Y., H.P., Y.X., J.F. and Z.Y.Z. co-wrote the manuscript. All authors contributed to the review and editing of the manuscript.

Competing interests

The authors declare no competing interests.

References

1. M. Rodell; J.S. Famiglietti; D.N. Wiese; J.T. Reager; H.K. Beaudoing; F.W. Landerer; M.H. Lo, Emerging Trends in Global Freshwater Availability. *Nature* **2018,** *557* (7707), 651-659.
2. S. Zhao; L. Zou; C.Y. Tang; D. Mulcahy, Recent Developments in Forward Osmosis: Opportunities and Challenges. *J. Membr. Sci.* **2012,** *396*, 1-21.
3. R. Wang; L. Shi; C.Y. Tang; S. Chou; C. Qiu; A.G. Fane, Characterization of Novel Forward Osmosis Hollow Fiber Membranes. *J. Membr. Sci.* **2010,** *355* (1), 158-167.
4. Y. Wang; Q. Pan; Y. Qiao; X. Wang; D. Deng; F. Zheng; B. Chen; J. Qiu, Layered Metal Oxide Nanosheets with Enhanced Interlayer Space for Electrochemical Deionization. *Adv. Mater.* **2023,** *35* (15), 2210871.
5. H.Y. Yang; Z.J. Han; S.F. Yu; K.L. Pey; K. Ostrikov; R. Karnik, Carbon Nanotube Membranes with Ultrahigh Specific Adsorption Capacity for Water Desalination and Purification. *Nat. Commun.* **2013,** *4*, 2220.
6. T.Y. Liu; J. Serrano; J. Elliott; X.Z. Yang; W. Cathcart; Z.X. Wang; Z. He; G.L. Liu, Exceptional Capacitive Deionization Rate and Capacity by Block Copolymer-based Porous Carbon Fibers. *Sci. Adv.* **2020,** *6* (16), eaaz0906.
7. S.-i. Jeon; H.-r. Park; J.-g. Yeo; S. Yang; C.H. Cho; M.H. Han; D.K. Kim, Desalination via a New Membrane Capacitive Deionization Process Utilizing Flow-electrodes. *Energy Environ. Sci.* **2013,** *6* (5), 1471-1475.
8. R. Ou; H. Zhang; V.X. Truong; L. Zhang; H.M. Hegab; L. Han; J. Hou; X. Zhang; A. Deletic; L. Jiang; G.P. Simon; H. Wang, A Sunlight-responsive Metal-organic Framework System for Sustainable Water Desalination. *Nat. Sustain.* **2020,** *3* (12), 1052-1058.
9. K. Zuo; X. Huang; X. Liu; E.M. Gil Garcia; J. Kim; A. Jain; L. Chen; P. Liang; A. Zepeda; R. Verduzco; J. Lou; Q. Li, A Hybrid Metal-Organic Framework-Reduced Graphene Oxide Nanomaterial for Selective Removal of Chromate from Water in an Electrochemical Process. *Environ. Sci. Technol.* **2020,** *54* (20), 13322-13332.
10. J.G. Gamaethiralalage; K. Singh; S. Sahin; J. Yoon; M. Elimelech; M.E. Suss; P. Liang; P.M. Biesheuvel; R.L. Zornitta; L.C.P.M. de Smet, Recent Advances in Ion Selectivity with Capacitive Deionization. *Energy Environ. Sci.* **2021,** *14* (3), 1095-1120.
11. J. Sun; S. Garg; T.D. Waite, A Novel Integrated Flow-Electrode Capacitive Deionization and Flow Cathode System for Nitrate Removal and Ammonia Generation from Simulated Groundwater. *Environ. Sci. Technol.* **2023,** *57* (39), 14726-14736.
12. M. Mao; T. Yan; J. Shen; J. Zhang; D. Zhang, Selective Capacitive Removal of Heavy

Metal Ions from Wastewater over Lewis Base Sites of S-Doped Fe–N–C Cathodes via an Electro-Adsorption Process. *Environ. Sci. Technol.* **2021,** *55* (11), 7665-7673.
13. M. Mao; T. Yan; G. Chen; J. Zhang; L. Shi; D. Zhang, Selective Capacitive Removal of Pb^{2+} from Wastewater over Redox-Active Electrodes. *Environ. Sci. Technol.* **2021,** *55* (1), 730-737.
14. P. Simon; Y. Gogotsi, Perspectives for electrochemical capacitors and related devices. *Nat. Mater.* **2020,** *19* (11), 1151-1163.
15. L. Wang; J.E. Dykstra; S.H. Lin, Energy Efficiency of Capacitive Deionization. *Environ. Sci. Technol.* **2019,** *53* (7), 3366-3378.
16. X. Xu; M. Eguchi; Y. Asakura; L. Pan; Y. Yamauchi, Metal–organic Framework Derivatives for Promoted Capacitive Deionization of oxygenated Saline Water. *Energy Environ. Sci.* **2023,** *16*, 1815-1820.
17. S. Kumar; N.M. Aldaqqa; E. Alhseinat; D. Shetty, Electrode materials for desalination of water via capacitive deionization. *Angew. Chem. Int. Ed. n/a* (n/a), e202302180.
18. Z.-H. Huang; Z. Yang; F. Kang; M. Inagaki, Carbon Electrodes for Capacitive Deionization. *J. Mater. Chem. A* **2017,** *5* (2), 470-496.
19. H. Peng; B. Yao; X. Wei; T. Liu; T. Kou; P. Xiao; Y. Zhang; Y. Li, Pore and Heteroatom Engineered Carbon Foams for Supercapacitors. *Adv. Energy Mater.* **2019,** *9* (19), 1803665.
20. X. Xu; Y. Liu; T. Lu; Z. Sun; D.H.C. Chua; L. Pan, Rational Design and Fabrication of Graphene/carbon Nanotubes Hybrid Sponge for High-performance Capacitive Deionization. *J. Mater. Chem. A* **2015,** *3* (25), 13418-13425.
21. H. Yin; S. Zhao; J. Wan; H. Tang; L. Chang; L. He; H. Zhao; Y. Gao; Z. Tang, Three-Dimensional Graphene/Metal Oxide Nanoparticle Hybrids for High-Performance Capacitive Deionization of Saline Water. *Adv. Mater.* **2013,** *25* (43), 6270-6276.
22. S. Cao; Y. Li; Y. Tang; Y. Sun; W. Li; X. Guo; F. Yang; G. Zhang; H. Zhou; Z. Liu; Q. Li; M. Shakouri; H. Pang, Space-Confined Metal Ion Strategy for Carbon Materials Derived from Cobalt Benzimidazole Frameworks with High Desalination Performance in Simulated Seawater. *Adv. Mater.* **2023,** *35* (23), 2301011.
23. L.L. Zhang; X.S. Zhao, Carbon-based Materials as Supercapacitor Electrodes. *Chem. Soc. Rev.* **2009,** *38* (9), 2520-2531.
24. Y. Gogotsi; P. Simon, True Performance Metrics in Electrochemical Energy Storage. *Science* **2011,** *334* (6058), 917-918.
25. Q. Li; X. Xu; J. Guo; J.P. Hill; H. Xu; L. Xiang; C. Li; Y. Yamauchi; Y. Mai, Two-Dimensional MXene-Polymer Heterostructure with Ordered In-Plane Mesochannels for High-Performance Capacitive Deionization. *Angew. Chem. Int. Ed.* **2021,** *60* (51), 26528-26534.
26. A.B. Fuertes; G. Lota; T.A. Centeno; E. Frackowiak, Templated Mesoporous Carbons for Supercapacitor Application. *Electrochim. Acta* **2005,** *50* (14), 2799-2805.
27. Y. Xia; T.S. Mathis; M.Q. Zhao; B. Anasori; A. Dang; Z.H. Zhou; H. Cho; Y. Gogotsi; S. Yang, Thickness -independent Capacitance of Vertically Aligned Liquid-crystalline MXenes. *Nature* **2018,** *557* (7705), 409-412.
28. X. Shen; Y. Xiong; R. Hai; F. Yu; J. Ma, All-MXene-Based Integrated Membrane Electrode Constructed using $Ti_3C_2T_x$ as an Intercalating Agent for High-Performance Desalination. *Environ. Sci. Technol.* **2020,** *54* (7), 4554-4563.
29. W.S. Chen; J.J. Gu; Q.L. Liu; M.Z. Yang; C. Zhan; X.N. Zang; T.A. Pham; G.X. Liu; W. Zhang; D. Zhang; B. Dunn; Y.M. Wang, Two-dimensional Quantum-sheet Films with Sub-1.2 nm Channels for Ultrahigh-rate Electrochemical Capacitance. *Nat. Nanotechnol.* **2022,** *17* (2), 153-158.
30. F. Xing; T. Li; J. Li; H. Zhu; N. Wang; X. Cao, Chemically Exfoliated MoS_2 for Capacitive Deionization of Saline Water. *Nano Energy* **2017,** *31*, 590-595.
31. V. Augustyn; Y. Gogotsi, 2D Materials with Nanoconfined Fluids for Electrochemical Energy Storage. *Joule* **2017,** *1* (3), 443-452.
32. L. Ding; L. Li; Y. Liu; Y. Wu; Z. Lu; J. Deng; Y. Wei; J. Caro; H. Wang, Effective Ion Sieving with $Ti_3C_2T_x$ MXene Membranes for Production of Drinking Water from Seawater.

Nat. Sustain. **2020,** *3* (4), 296-302.
33. W. Wang; N. Onofrio; E. Petit; B.A. Karamoko; H. Wu; J. Liu; J. Li; K. Qi; Y. Zhang; C. Gervais; L. Lajaunie; C. Salameh; P. Miele; Z. Zeng; D. Voiry, High-surface-area Functionalized Nanolaminated Membranes for Energy-efficient Nanofiltration and Desalination in Forward Osmosis. *Nat. Water.* **2023,** *1* (2), 187-197.
34. L. Mei; Z. Cao; T. Ying; R. Yang; H. Peng; G. Wang; L. Zheng; Y. Chen; C.Y. Tang; D. Voiry; H. Wang; A.B. Farimani; Z. Zeng, Simultaneous Electrochemical Exfoliation and Covalent Functionalization of MoS_2 Membrane for Ion Sieving. *Adv. Mater.* **2022,** *34* (26), 2201416.
35. X. Zhao; S. Ning; W. Fu; S.J. Pennycook; K.P. Loh, Differentiating Polymorphs in Molybdenum Disulfide via Electron Microscopy. *Adv. Mater.* **2018,** *30* (47), 1802397.
36. Z. Lai; Q. He; T.H. Tran; D.V.M. Repaka; D.-D. Zhou; Y. Sun; S. Xi; Y. Li; A. Chaturvedi; C. Tan; B. Chen; G.-H. Nam; B. Li; C. Ling; W. Zhai; Z. Shi; D. Hu; V. Sharma; Z. Hu; Y. Chen; Z. Zhang; Y. Yu; X. Renshaw Wang; R.V. Ramanujan; Y. Ma; K. Hippalgaonkar; H. Zhang, Metastable 1T′-phase group VIB transition metal dichalcogenide crystals. *Nat. Mater.* **2021,** *20* (8), 1113-1120.
37. Y. Yu; G.-H. Nam; Q. He; X.-J. Wu; K. Zhang; Z. Yang; J. Chen; Q. Ma; M. Zhao; Z. Liu; F.-R. Ran; X. Wang; H. Li; X. Huang; B. Li; Q. Xiong; Q. Zhang; Z. Liu; L. Gu; Y. Du; W. Huang; H. Zhang, High phase-purity 1T′-MoS_2- and 1T′-$MoSe_2$-layered crystals. *Nature Chemistry* **2018,** *10* (6), 638-643.
38. M. Acerce; D. Voiry; M. Chhowalla, Metallic 1T Phase MoS_2 Nanosheets as Supercapacitor Electrode Materials. *Nat. Nanotechnol.* **2015,** *10* (4), 313-318.
39. Z. Zeng; Z. Yin; X. Huang; H. Li; Q. He; G. Lu; F. Boey; H. Zhang, Single-Layer Semiconducting Nanosheets: High-Yield Preparation and Device Fabrication. *Angew. Chem. Int. Ed.* **2011,** *50* (47), 11093-11097.
40. R. Yang; L. Mei; Q. Zhang; Y. Fan; H.S. Shin; D. Voiry; Z. Zeng, High-yield Production of Mono- or Few-layer Transition Metal Dichalcogenide Nanosheets by an Electrochemical Lithium Ion Intercalation-based Exfoliation Method. *Nat. Protoc.* **2022,** *17* (2), 358-377.
41. R. Yang; Y. Fan; L. Mei; H.S. Shin; D. Voiry; Q. Lu; J. Li; Z. Zeng, Synthesis of Atomically Thin Sheets by the Intercalation-based Exfoliation of Layered Materials. *Nat. Synth.* **2023,** *2* (2), 101-118.
42. J.N. Coleman; M. Lotya; A. O'Neill; S.D. Bergin; P.J. King; U. Khan; K. Young; A. Gaucher; S. De; R.J. Smith; I.V. Shvets; S.K. Arora; G. Stanton; H.-Y. Kim; K. Lee; G.T. Kim; G.S. Duesberg; T. Hallam; J.J. Boland; J.J. Wang; J.F. Donegan; J.C. Grunlan; G. Moriarty; A. Shmeliov; R.J. Nicholls; J.M. Perkins; E.M. Grieveson; K. Theuwissen; D.W. McComb; P.D. Nellist; V. Nicolosi, Two-Dimensional Nanosheets Produced by Liquid Exfoliation of Layered Materials. *Science* **2011,** *331* (6017), 568-571.
43. Z. Shi; X. Zhang; X. Lin; G. Liu; C. Ling; S. Xi; B. Chen; Y. Ge; C. Tan; Z. Lai; Z. Huang; X. Ruan; L. Zhai; L. Li; Z. Li; X. Wang; G.-H. Nam; J. Liu; Q. He; Z. Guan; J. Wang; C.-S. Lee; A.R.J. Kucernak; H. Zhang, Phase-dependent Growth of Pt on MoS_2 for Highly Efficient H_2 Evolution. *Nature* **2023,** *621* (7978), 300-305.
44. L. Ries; E. Petit; T. Michel; C.C. Diogo; C. Gervais; C. Salameh; M. Bechelany; S. Balme; P. Miele; N. Onofrio; D. Voiry, Enhanced Sieving from Exfoliated MoS_2 Membranes via Covalent Functionalization. *Nat. Mater.* **2019,** *18* (10), 1112-1117.
45. M.E. Suss; S. Porada; X. Sun; P.M. Biesheuvel; J. Yoon; V. Presser, Water Desalination via Capacitive Deionization: what is it and what can we expect from it? *Energy Environ. Sci.* **2015,** *8* (8), 2296-2319.
46. X. Yang; C. Cheng; Y. Wang; L. Qiu; D. Li, Liquid-Mediated Dense Integration of Graphene Materials for Compact Capacitive Energy Storage. *Science* **2013,** *341* (6145), 534-537.
47. J. Han; T. Yan; J. Shen; L. Shi; J. Zhang; D. Zhang, Capacitive Deionization of Saline Water by Using MoS_2-Graphene Hybrid Electrodes with High Volumetric Adsorption Capacity. *Environ. Sci. Technol.* **2019,** *53* (21), 12668-12676.

48. C. Zhan; Y. Sun; F. Aydin; Y.M. Wang; T.A. Pham, Confinement Effects on the Solvation Structure of Solvated Alkaline Metal Cations in a Single-digit 1T-MoS_2 Nanochannel: A First-principles Study. *J. Chem. Phys.* **2021,** *154* (16).
49. G. Kresse; D. Joubert, From Ultrasoft Pseudopotentials to the Projector Augmented-wave Method. *Phys. Rev. B* **1999,** *59* (3), 1758-1775.
50. G. Kresse; J. Furthmüller, Efficient Iterative Schemes for ab initio Total-energy Calculations using a Plane-wave Basis Set. *Phys. Rev. B* **1996,** *54* (16), 11169-11186.
51. G. Kresse; J. Furthmüller, Efficiency of ab-initio Total Energy Calculations for Metals and Semiconductors using a Plane-wave Basis Set. *Comput. Mater. Sci.* **1996,** *6* (1), 15-50.
52. J.P. Perdew; K. Burke; M. Ernzerhof, Generalized Gradient Approximation Made Simple. *Phys. Rev. Lett.* **1996,** *77* (18), 3865-3868.
53. P.E. Blöchl, Projector Augmented-wave Method. *Phys. Rev. B* **1994,** *50* (24), 17953-17979.
54. S. Grimme, Semiempirical GGA-type Density Functional Constructed with a Long-range Dispersion Correction. *J. Comput. Chem.* **2006,** *27* (15), 1787-1799.
55. K. Mathew; R. Sundararaman; K. Letchworth-Weaver; T.A. Arias; R.G. Hennig, Implicit Solvation Model for Density-functional Study of Nanocrystal Surfaces and Reaction Pathways. *J. Chem. Phys.* **2014,** *140* (8).
56. K. Mathew; V.S.C. Kolluru; S. Mula; S.N. Steinmann; R.G. Hennig, Implicit Self-consistent Electrolyte Model in Plane-wave Density-functional Theory. *J. Chem. Phys.* **2019,** *151* (23).

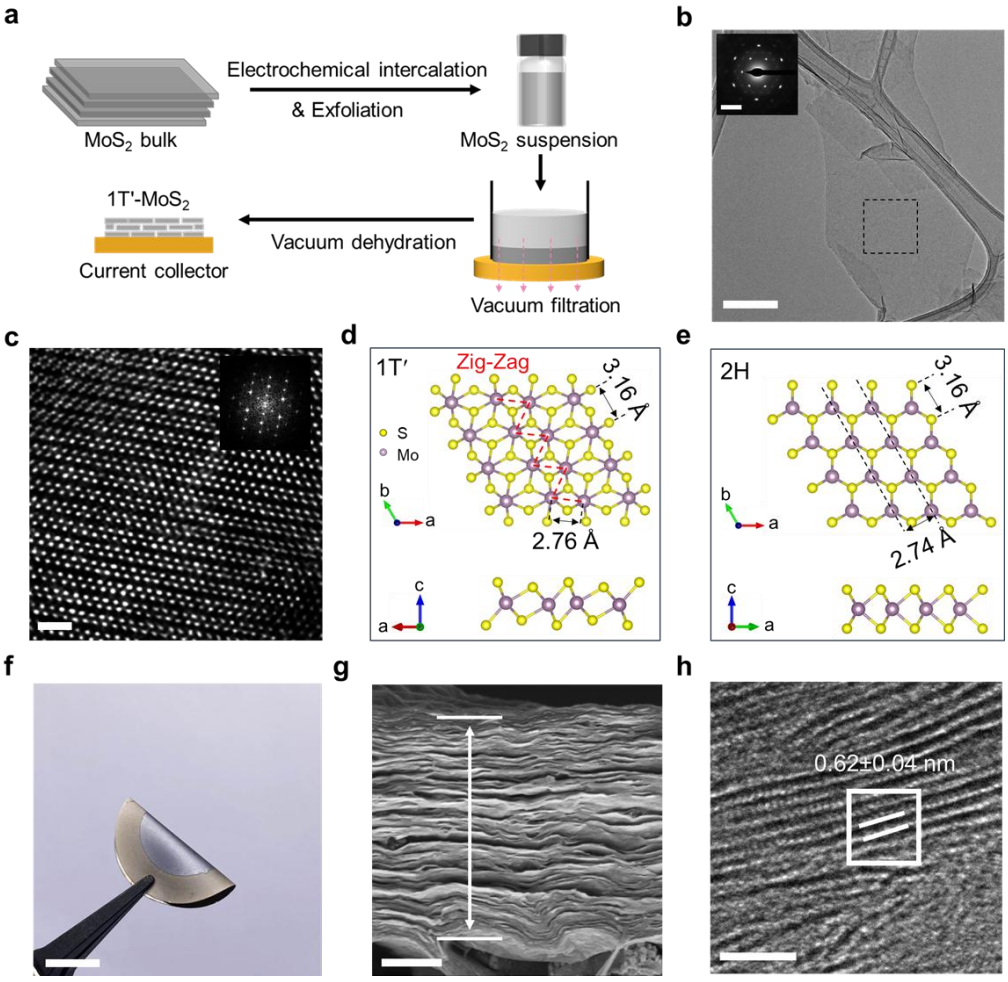

Figure 1 | Fabrication and electron microscopy characterizations of 1T′-MoS_2 nanosheets and electrode. a, Schematic illustration of the fabrication of 1T′-MoS_2 nanosheets and electrode *via* electrochemical lithium intercalation-based exfoliation method and vacuum filtration method (onto Au-coated PVDF substrate). **b**, TEM image of the exfoliated MoS_2 nanosheets. Scale bar, 200 nm. **Inset**, SAED pattern of the area denoted by black dashed rectangular box. Scale bar, 5 1/nm. **c**, HAADF-STEM image of the exfoliated1T′-MoS_2 nanosheets. Scale bar, 1 nm. **Inset**, the corresponding fast Fourier transform (FFT) pattern. Schematic illustrations of the atomic structures of **d**, 1T′-MoS_2 and **e**, 2H-MoS_2, respectively. The red dashed lines in **d** demonstrate the zig-zag chain of Mo atoms in 1T′-MoS_2. **f**, Photo of a 1T′-MoS_2 membrane fabricated by vacuum filtration with good flexibility. Scale bar: 1 cm. **g**, Cross-section SEM view of 1T′-MoS_2 electrode prepared by vacuum filtration, showing compact lamellar architecture. Scale bar: 300 nm. **h**, Cross-sectional TEM observations of horizontal 1T′-MoS_2 laminates with the separation of approximately 0.62 nm. Scale bar: 5 nm.

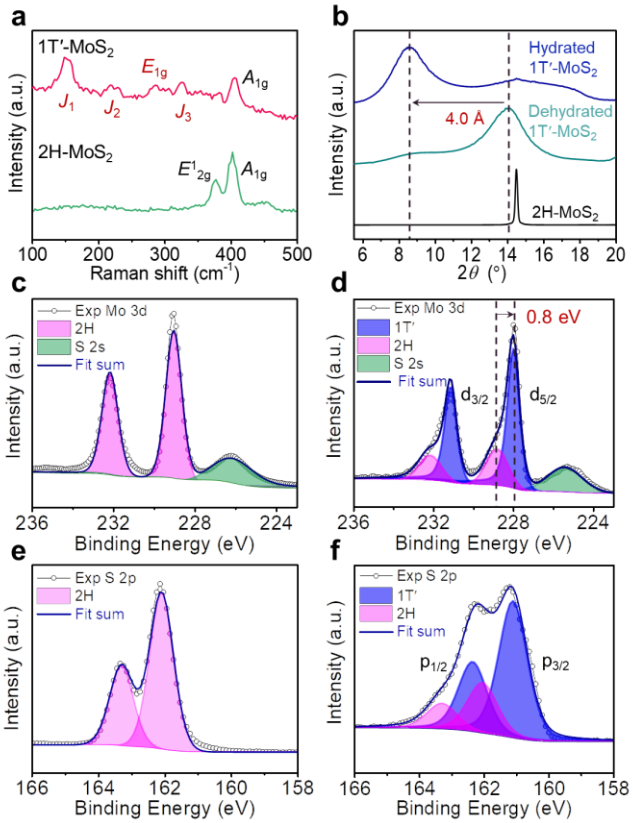

Figure 2 | Raman, XRD, and XPS characterization of 1T′- and 2H-MoS_2 electrodes. **a**, Raman spectroscopy. The 1T′-MoS_2 electrode shows distinctive Raman modes of J_1, J_2, J_3 and E_{1g}. **b**, XRD patterns of the hydrated and dehydrated 1T′-MoS_2 and 2H-MoS_2 electrodes. Hydration gives rise to the enlarged interlayer spacing of 1T′-MoS_2 electrode with approximately 4.0 Å. XPS spectra of 2H-MoS_2 electrode (**c**, Mo 3d and **e**, S 2p) and 1T′-MoS_2 electrode (**d**, Mo 3d, **f**, S 2p). The characteristic peaks of the 1T′ phase shifted to lower value by approximately 0.8 eV compared with the 2H phase. **a.u.**, arbitrary units.

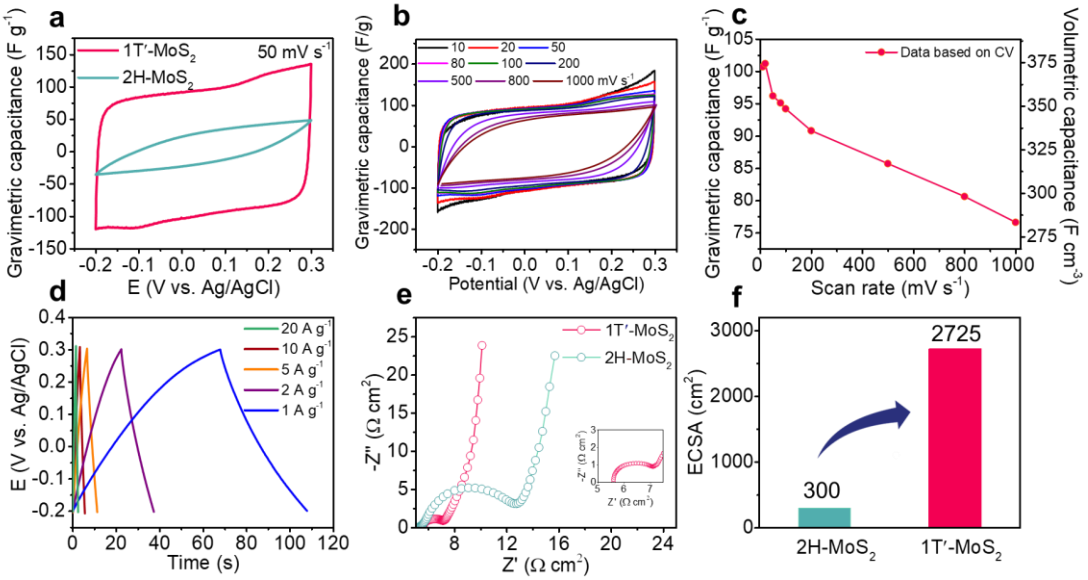

Figure 3 | Electrochemical properties of the 1T′-MoS_2 electrode in 1 M KCl electrolyte. a, Cyclic voltammograms of 2H and 1T′-MoS_2 electrodes with the scan rate of 50 mV s^{-1}. The 1T′-MoS_2 electrode shows the near-rectangular and symmetric curves with EDLC behavior compared to the less favorable shape of 2H-MoS_2 electrode. **b**, Cyclic voltammograms of 1T′-MoS_2 electrode over scan rates from 10 to 1000 mV s^{-1}, showing the excellent and stable performance of 1T′-MoS_2 electrode even at an ultrahigh scan rate. **c**, Gravimetric capacitance and volumetric capacitance of 1T′-MoS_2 electrode decreased with increased scan rates. **d**, Galvanostatic charge-discharge (GCD) data of 1T′-MoS_2 electrode collected from 1 to 20 A g^{-1}. **e**, Electrochemical Impedance Spectroscopy (EIS) data for the 1T′-MoS_2 and 2H-MoS_2 electrodes. **Inset,** the zoom-in data of EIS result for 1T′-MoS_2 electrode. **f**, Calculated electrochemical active surface area (ECSA) for 2H and 1T′-MoS_2 electrodes: demonstrating nearly ten-fold larger ECSA value for 1T′-MoS_2 compared with 2H-MoS_2 electrode.

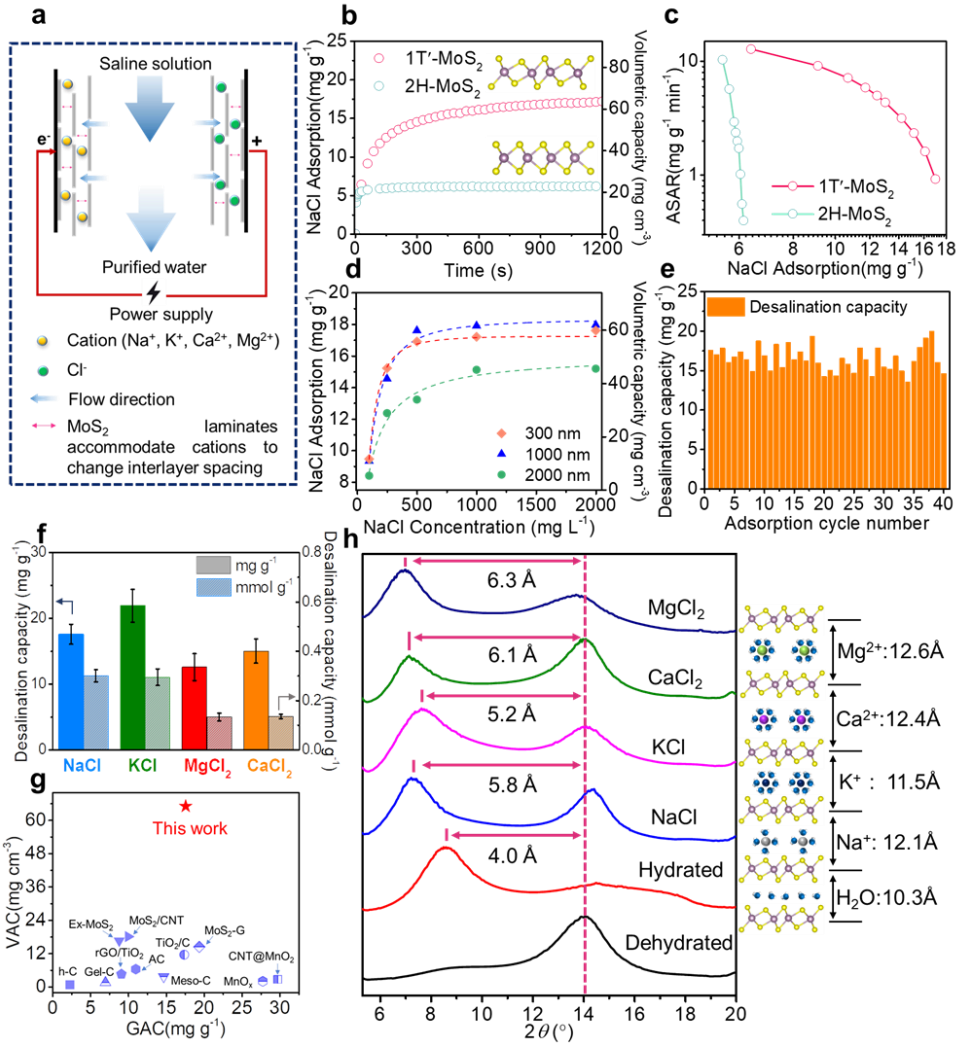

Figure 4 | Capacitive desalination performances and mechanism study. a, Schematic illustration of CDI working mechanism. **b**, Typical time-resolved gravimetric adsorption capacities (GAC) profiles of 1T′-MoS_2 and 2H-MoS_2 electrodes in 500 mg L^{-1} NaCl solution. **c**, Kim-Yoon CDI Ragone diagram of 1T′-MoS_2 in contrast with 2H-MoS_2 electrode. **d**, GAC of 1T′-MoS_2 electrode with respect to different initial concentration of NaCl solution. Dashed lines represent the Langmuir fitting of the adsorption isotherm data. Error bars are omitted for clarity. **e**, Repeated adsorption-desorption cycles for NaCl desalination of the 1T′-MoS_2 electrode. **f**, GAC and molar desalination capacities of 1T′-MoS_2 electrode for NaCl, KCl, $MgCl_2$, and $CaCl_2$ deionization. Error bars represent **s. d.** of three independent measurements. **g**, Comparison of volumetric adsorption capacities (VAC) versus GAC of reported state-of-the-art materials and MoS_2 laminates of this work. The detailed data of literature are listed in **Table S2**. **h**, *Ex situ* XRD patterns of restacked 1T′ phase MoS_2 electrode

immersed in different saline solutions. The enlarged interlayer spacing of electrodes are denoted on the right for clarification with respective cations and water molecule, showing the dynamic accommodation effect of MoS_2 nanochannels.

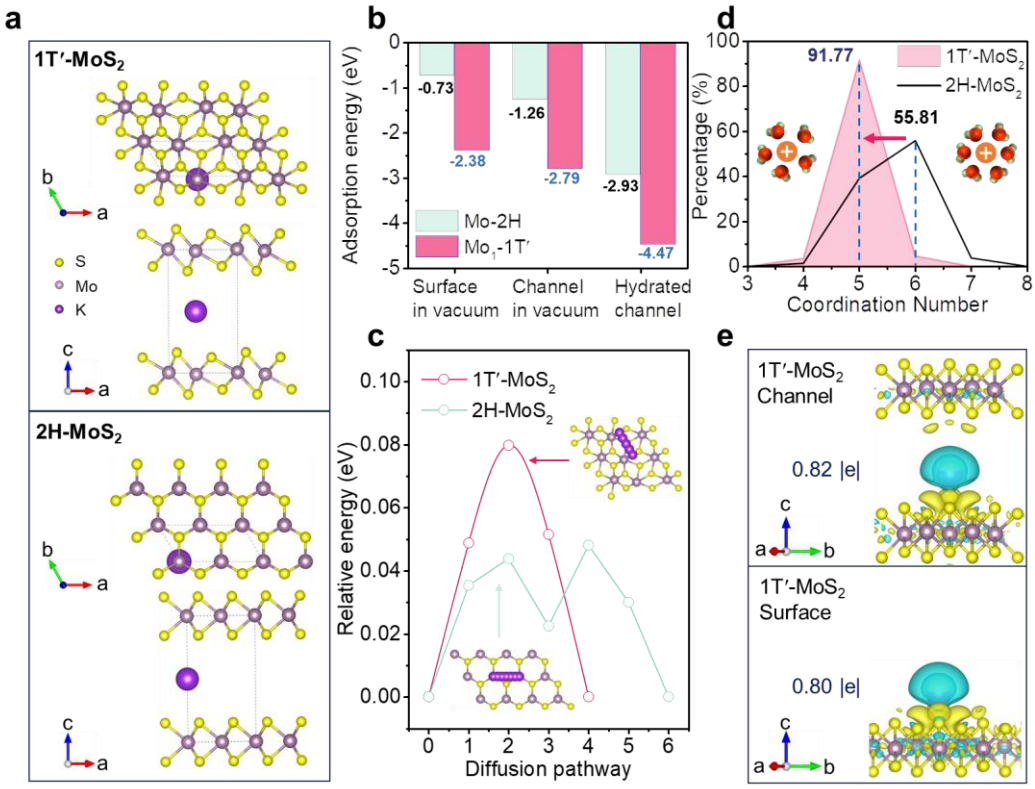

Figure 5 | DFT calculations and AIMD simulations of the interaction between K^+ and MoS_2. a, Schematic illustrations of atomic structures of preferred K^+ adsorbed position on the basal plane of 1T′-MoS_2, 2H-MoS_2 (denoted as Mo_1-1T′, Mo-2H) and in the respective 2D channels. **b**, Interaction energy of K^+-MoS_2 with the conditions of MoS_2 surface in vacuum, MoS_2 channels in vacuum and hydrated MoS_2 channels. We selected the most stable initial sites for comparison. **c**, Migration energies of K^+ when diffusing *via* possible pathway on the surface. **Inset**, possible diffusion pathway for 2H and 1T′-MoS_2 surface. **d**, Probability partition of the cation's coordination number with water in the 2H and 1T′-MoS_2 channels. **e**, The charge density difference of K^+ in the channel and surface of 1T′-MoS_2, and the corresponding charge transfer from metal to the channel. The isosurface level is set as 0.001 e $Å^{-3}$.

Supplementary Information

for

Achieving Exceptional Volumetric Desalination Capacity Using Compact MoS_2 Nanolaminates

Ting Ying[1]†, Yu Xiong[1]†, Huarong Peng[1]†, Ruijie Yang[1], Liang Mei[1], Zhen Zhang[1], Weikang Zheng[1], Ruixin Yan[1], Yue Zhang[1], Honglu Hu[1], Chen Ma[2], Ye Chen[2], Xingtao Xu[3], Juan Yang[4], Damien Voiry[5], Chuyang Y. Tang[6], Jun Fan[1], Zhiyuan Zeng[1,7*]

[1]Department of Materials Science and Engineering, and State Key Laboratory of Marine Pollution, City University of Hong Kong, 83 Tat Chee Avenue, Kowloon, Hong Kong S.A.R. 999077, P. R. China.

[2]Department of Chemistry, The Chinese University of Hong Kong, Hong Kong S.A.R. 999077, China.

[3]Marine Science and Technology College, Zhejiang Ocean University, Zhoushan, Zhejiang 316022, China.

[4]School of Chemical Engineering and Technology, Xi'an Jiaotong University, Xi'an, 710049 China.

[5]Institut Européen des Membranes, IEM, UMR 5635, Université Montpellier, ENSCM, CNRS, Montpellier 34000, France.

[6]Department of Civil Engineering, The University of Hong Kong, Hong Kong S.A.R. 999077, China.

[7]Shenzhen Research Institute, City University of Hong Kong, Shenzhen 518057, P. R. China.

†These authors contributed equally to this work.

[*]Corresponding authors: zhiyzeng@cityu.edu.hk (Z. Y. Zeng)

Contents

22. Atomic model of 1T′-MoS_2 and 2H-MoS_2 channels: **Figure S20**

23. Ion-MoS_2 interaction for 1T′-MoS_2 and 2H-MoS_2 channels when potassium ion resides in different initial positions: **Table S3**

24. Snapshots of a solvated potassium ion in MoS_2 channel with respective time sequences: **Figure S21-Figure S22**

25. Interfacial partial charge transfer comparison: **Figure S23**

Supplementary Methods

Chemicals. The MoS_2 bulk powder (Macklin), carbon black (CABOT BP2000), poly(vinylidene fluoride) (PVDF, Sigma Aldrich), *N*-methylpyrrolidone (NMP, Sigma Aldrich), Polypropylene film (pp, Celgard 2300), Nylon or PVDF filter membrane purchased from ALADDIN. Reagents such as sodium chloride (NaCl), potassium chloride (KCl), magnesium Chloride, hexahydrate ($MgCl_2.6H_2O$), calcium chloride ($CaCl_2$) and sucrose were purchased from ALADDIN. All chemicals were used as received.

Characterization. Transmission electron microscopy (TEM, JEM 2100F), scanning electron microscopy (SEM, TESCAN MIRA4). X-ray photoelectron spectroscopy (XPS, Thermo Scientific K-Alpha Nexsa). All XPS data were calibrated using the C 1s peak (284.8 eV) of adventitious carbon with the peak fitting operated *via* Thermo Avantage software. XPS depth profile was collected in between each etch step using the Ar^+ etching source with relative depth of 30, 60 and 90 nm. The relative depth was evaluated by comparing the time taken for etching standard Ta_2O_5 samples. Raman spectroscopy (WITec alpha 300 confocal Raman microscope, 532 nm excitation wavelength), and X-ray diffraction (XRD, Bruker D2 PHASER, λ = 1.54 Å). The zeta potential of nanosheets suspension was measured on the Malvern Zetasizer Nano series at neutral pH. The contact angles of electrodes were carried out on OCA 15EC Contact Angle Tester repeating three times. When conducting XRD measurements on the membrane immersed in salt solutions and DI water, the membrane was carefully removed from the solution using absorbent paper. Following this, XRD measurements were immediately performed.

Capacitance Calculations. For the three-electrode system, the gravimetric capacitance can be calculated from the CV data by using Equation (1).

$$C_g = \frac{\int IdV}{Vsm} \tag{1}$$

Where C_g is the gravimetric capacitance ($F\ g^{-1}$), I is the current (A), V is the scan potential range (V), s is the scan rate ($V\ s^{-1}$) and m is the weight of the active material (g).

Batch-Mode CDI Experiments. The batch-mode CDI experiments are carried out in a

custom-made electrochemical cell filled with 20 mL saline solution at room temperature with the variation less than 0.2 ºC. The symmetric electrode system was assembled using as-prepared electrodes, then immersed in solution to serve as working and counter electrodes. A conductivity meter (SevenMulti, METTLER TOLEDO, America) was used to monitor the conductivity of the NaCl solution in real time. The desalination potential was set at 0.5 V to avoid hydrogen evolution reaction. Before desalination, the two electrodes were soaked in the salt solution without an external bias to stabilize the solution conductivity and minimize the influence of initial physisorption. The weight of testing MoS_2 electrodes was around 1 mg.

CDI performance calculation. Desalination capacity such as volumetric capacity (Γ_V, $mg_{MCl}\ m^{-3}$), and gravimetric capacity (Γ_g, $mg_{MCl}\ g^{-1}$) with average salt adsorption rate (v, $mg_{MCl}\ g^{-1}\ min^{-1}$) are calculated according to the following equations,

$$\Gamma_g = \frac{(C_0 - C_t)\,V}{m} \tag{2}$$

$$\Gamma_V = \Gamma_g \times \rho \tag{3}$$

$$v = \frac{\Gamma}{t} \tag{4}$$

where C_0 and C_t represent the initial and final solution concentrations, respectively. V is the volume of saline solutions (20 mL); MCl stands for different saline solution, i.e., (NaCl, KCl, $MgCl_2$, $CaCl_2$). m is the total mass of the active materials loaded on two electrodes, t is the charging time, ρ is the density of MoS_2 electrodes. The electrodes were immersed in saline solution before measurements to preclude the effects of physical adsorption of NaCl.

Electrochemically Active Surface Area *(ECSA).* To measure the electrochemical capacitance, the potential was swept between -0.2 and 0.3 V versus Ag/AgCl three times at each of different scan rates (10, 20, 50, 80, 100 mV s^{-1}). We measured the capacitive currents in which no faradic processes are observed, i.e., at 0.05 V versus Ag/AgCl. The specific capacitance can be converted into an ECSA using the specific capacitance value for a flat standard with 1 cm^2 of real surface area[1]. The specific capacitance for a flat surface is generally found to be in the range of 20-60 μF cm^{-2}. Here we assume the value of 40 μF cm^{-2} for following calculation[1]. Calculated electrochemical active surface area:

$$A_{ECSA} = \frac{\text{specific capacitance}}{40\ \text{F cm}^{-2}\ \text{per cm}^2_{ECSA}} \quad (5)$$

1

2

Supplementary Figures

Characterization of original MoS_2 powder and 2H-MoS_2 electrode

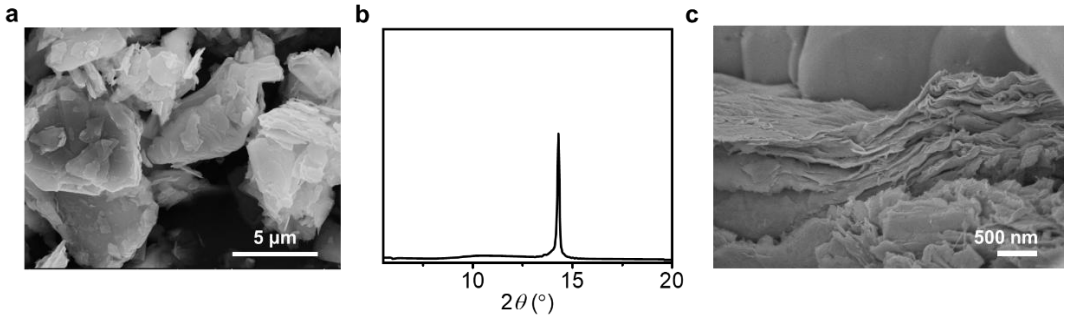

Figure S1 | a, SEM image of MoS_2 bulk powder. **b**, XRD pattern of bulk powder. **c**, Cross-view of 2H-MoS_2 electrode, exhibiting typical laminated structure.

Zeta potential measurements

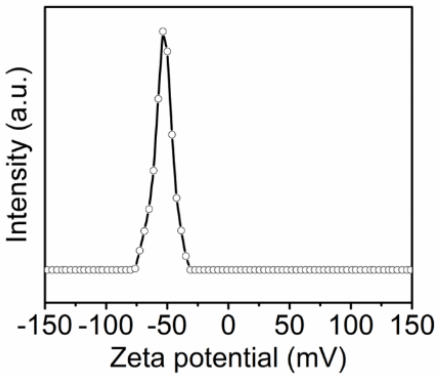

Figure S2 | a, Zeta potential of MoS_2 aqueous suspension under neutral condition. The Zeta potential value of -53.2 mV shows the negative nature of exfoliated MoS_2 nanosheets.

AFM imaging of MoS_2 nanosheets

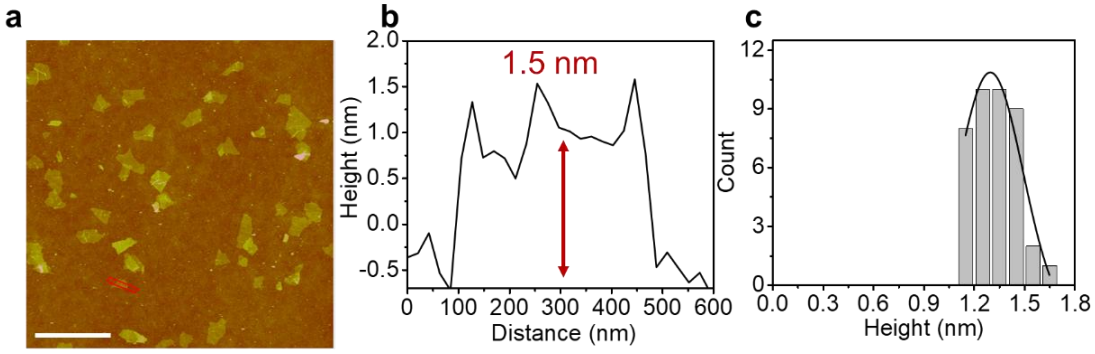

Figure S3 | a, AFM image of exfoliated MoS_2 nanosheets. Scale bar, 2 μm. **b**, measured thickness of the nanosheets denoted by red dashed box in (**a**). **c**, the statistical analysis of thickness of exfoliated MoS_2 nanosheets by measuring 40 pieces.

STEM Characterization of MoS_2 nanosheets

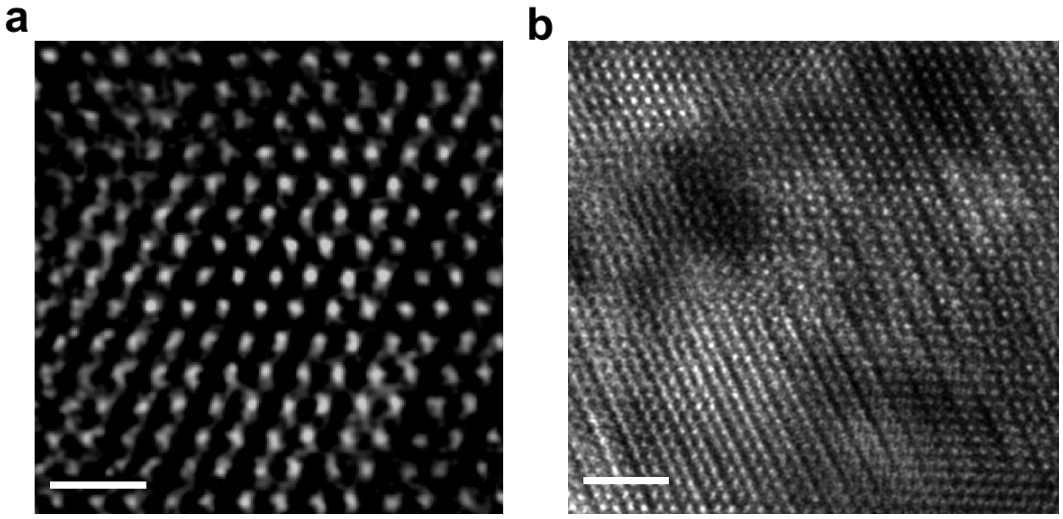

Figure S4 | High-angle annular dark-field scanning transmission electron microscopy (HAADF-STEM) images of 1T′-MoS_2 of different areas. Scale bar, **a**, 1 nm and **b**, 3 nm.

STEM analysis of 1T'-MoS_2 nanosheets and Mo-Mo distance

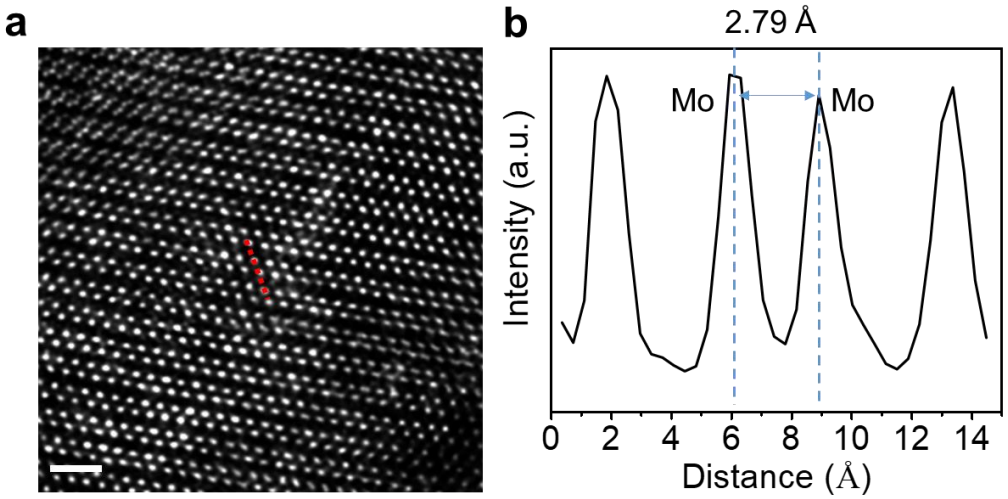

Figure S5 | High-angle annular dark-field scanning transmission electron microscopy (HAADF-STEM) image analysis of 1T′-MoS_2. **a**, HAADF-STEM image of 1T′-MoS_2. **Inset**, scale bar, 1 nm. **b**, The corresponding intensity profile of the red dotted line in **a**. The Mo-Mo distance is 2.79 Å in this case.

Comparison of 2H and 1T'-MoS_2 nanosheets

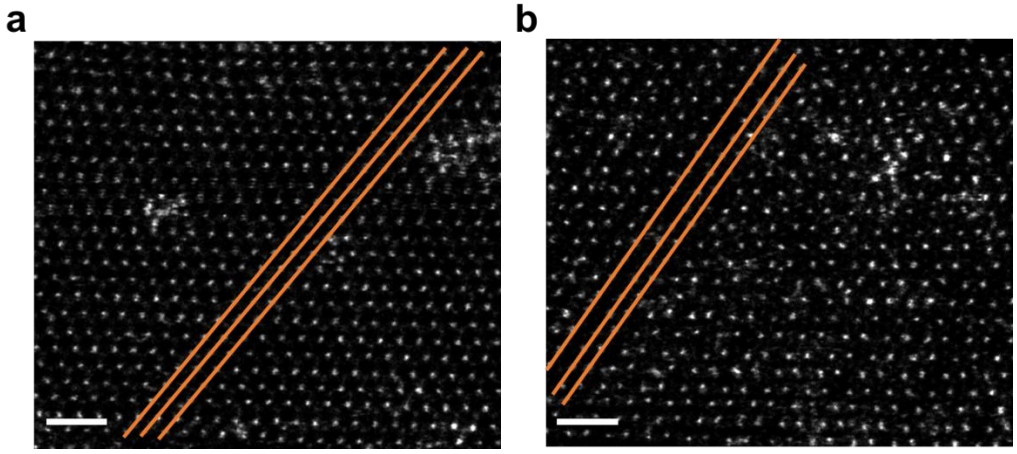

Figure S6 | High-angle annular dark-field scanning transmission electron microscopy (HAADF-STEM) image analysis of **a**, 2H-MoS_2 and **b**, 1T′-MoS_2. Scale bar, 1 nm.

The intercalation of lithium ions into layered MoS_2 involves electron transfers from the *s* orbital of lithium ions into the *d* orbital of the host transition metal (Mo) to maintain overall charge neutrality[2]. When the electron transfers beyond a certain threshold (for MoS_2, this threshold is 0.29 electrons per formula unit[3]), the stability of the metal coordination structure of trigonal prismatic (2H phase) will be lower than that of the octahedral (1T phase), and thereby the in-plane bonding reconstructions and 2H-to-1T phase transitions will occur. The octahedral coordination (1T phase) can spontaneously distort to form distorted octahedral coordination structure (1T′ phase). Therefore, the overall phase transitions of MoS_2 induced by the intercalation of lithium ions are 2H-to-1T′.

Cross-section of MoS_2 electrodes with different thickness

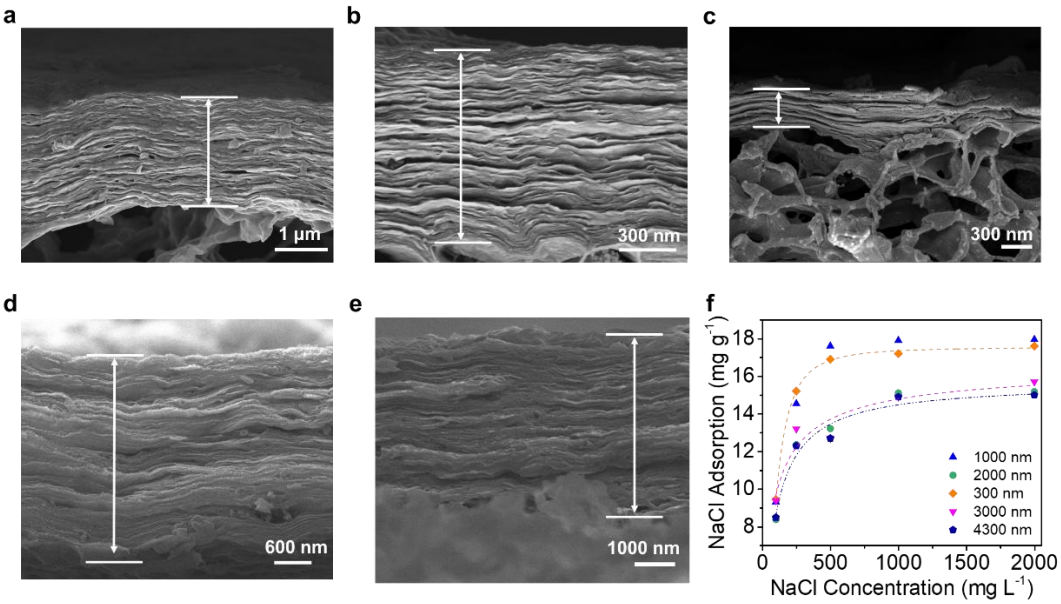

Figure S7 | Cross-view of 1T′-MoS_2 laminated electrodes with different thickness. **a**, 2000 nm. **b**, 1000 nm. **c**, 300 nm. **d**, 3000 nm. **e**, 4300 nm. **f**, GAC of 1T′-MoS_2 electrode with respect to different initial concentration of NaCl solution. Dashed lines represent the Langmuir fitting of the adsorption isotherm data. Error bars are omitted for clarity.

As shown in **Figure S7f**, all the GAC of electrodes with different thicknesses (300, 1000, 2000 nm, 3000 nm, 4300 nm) follow the Langmuir adsorption isotherm representing the relationship between the quantity of adsorbed salt and the NaCl initial concentration (dashed lines). We found that the thickness of the electrodes influenced the adsorbed quantities. Obviously, too thick nanochannels may introduce resistance in cation transport, thereby reducing the overall adsorption capacity. When increasing the NaCl initial concentration from 1000 to 2000 mg L^{-1}, the NaCl adsorption reaches saturation, of which the value is inversely related with the increased thickness.

Surface morphology and roughness of 1T'-MoS_2 electrode

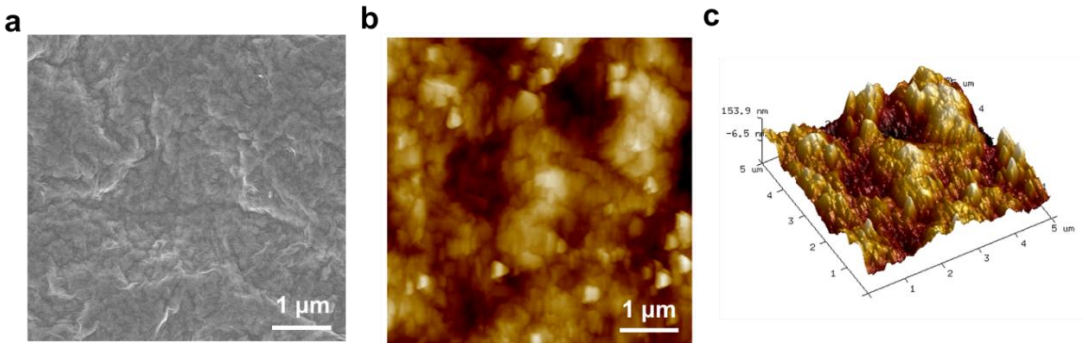

	1T′-MoS_2 electrodes
R_q (nm)	46.3
R_a (nm)	36.8

Figure S8 | a, Top-view of the 1T′ -MoS_2 electrode with flat surface. **b**, 2D and **c**, 3D AFM images of surface morphology of the MoS_2 electrode with a scan area of 5 μm×5 μm. The table below shows the surface roughness parameters of the MoS_2 electrode. R_q, root means square roughness, R_a, average roughness.

UV-Vis absorption spectra of 1T'-MoS_2 and 2H-MoS_2 dispersion

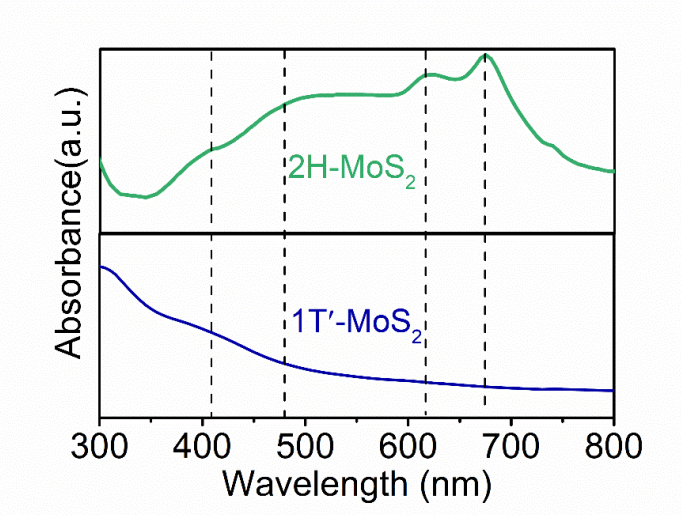

Figure S9 | Ultraviolet-visible (UV-Vis) absorption spectra of the 1T′-MoS_2 and 2H-MoS_2 dispersed in aqueous solution. Characteristic peaks of 2H-MoS_2 are clearly observed in the UV-Vis absorption spectrum as denoted by the black dashed lines.

Contact angle measurements

Figure S10 | The evolution of contact angle measurements of MoS_2 electrodes with time flies. The decreased values of contact angle strongly confirm the hydrophilicity of 1T′-MoS_2 electrode. **a**, snapshot at 0 s with contact angle of 58.7°. **b**, snapshot at 30 s with contact angle of 47.6°. **c**, snapshot at 70 s with contact angle of 30°.

XPS data for Mo 3d of 1T'-MoS_2 electrode

Table S1 XPS data for Mo 3d of 1T′-MoS_2 electrode

No.	Name	Peak BE (eV)	Height CPS	Height Ratio	Area CPS	Area Ratio	FWHM param (eV)
A	S 2s	224.73	8176.45	0.18	18516.5	0.43	2.18
B	Mo3d 1T′-MoS_2	227.3	45307.77	1	43153.22	1	0.74
C	Mo3d 1T′-MoS_2	230.44	31262.36	0.69	29666.17	0.69	0.74
D	Mo3d 2H-MoS_2	228.11	11953.91	0.26	16846.4	0.39	1.35
E	Mo3d 2H-MoS_2	231.46	8248.2	0.18	11622.55	0.27	1.35

Cyclic voltammograms of 2H-MoS_2 electrode at different scan rates

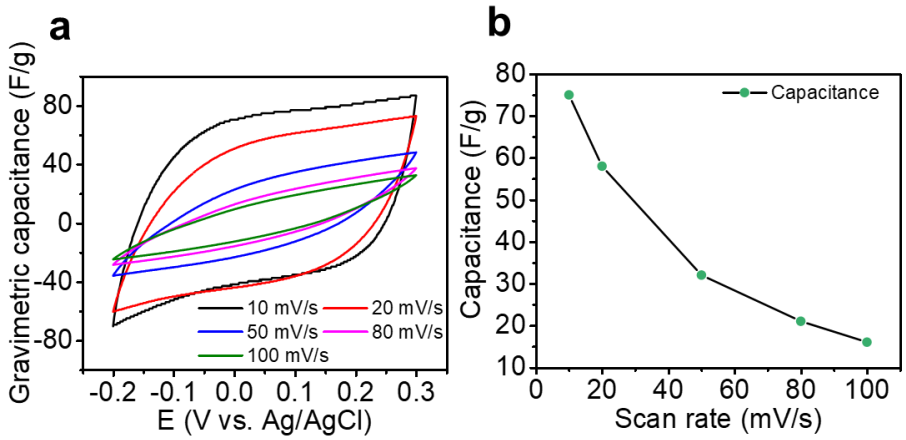

Figure S11 | a, CV curves of 2H-MoS_2 electrode with the scan rates of 10 mV/s, 20 mV/s, 50 mV/s, 80 mV/s and 100 mV/s. **b**, the gravimetric capacitance decreased with elevated scan rates. The shapes in **a** distorted severely when scan rate exceeds 50 mV/s, indicating 2H-MoS_2 is not suitable for high-rate charge and discharge.

ECSA linear curves of 2H-MoS_2 and 1T'-MoS_2 electrode

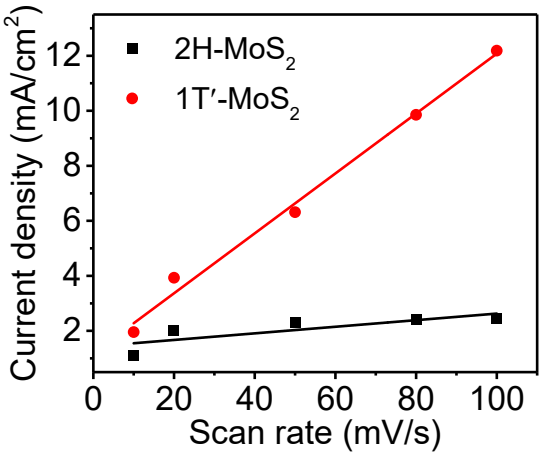

Figure S12 | The area current density related with scan rate for 1T′ and 2H MoS_2 electrode. We measured the capacitive currents in which no faradic processes are observed, i.e., at 0.05 V versus Ag/AgCl. The specific capacitance can be converted into an ECSA using the specific capacitance value for a flat standard with 1 cm^2 of real surface area. The specific capacitance for a flat surface is generally found to be in the range of 20-60 μF cm^{-2}. Here we assume the value of 40 μF cm^{-2} for the following calculation. The calculated capacitances of 1T′ and 2H MoS_2 are 109 and 12 mF cm^{-2}, respectively.

Therefore, ECSA $_{1T' MoS2}$=109 mF cm^{-2}/40 μF cm^{-2} per cm^2_{ECSA}=2725 cm^2_{ECSA}

ECSA $_{2H MoS2}$ =12 mF cm^{-2}/40 μF cm^{-2} per cm^2_{ECSA} = 300 cm^2_{ECSA}

Schematic representation of CDI Measurements setting

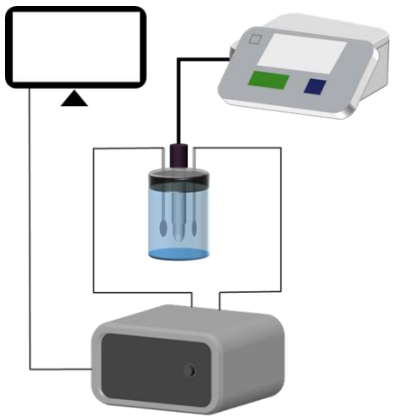

Figure S13 | Schematic representation of CDI Measurements setting. Electrochemical workstation was connected to the custom-made device and the concentration changes were monitored by the conductivity meter and can be converted by calibration curves shown in **Figure S14**.

Calibration curves of NaCl, $CaCl_2$, KCl, and $MgCl_2$ aqueous solutions

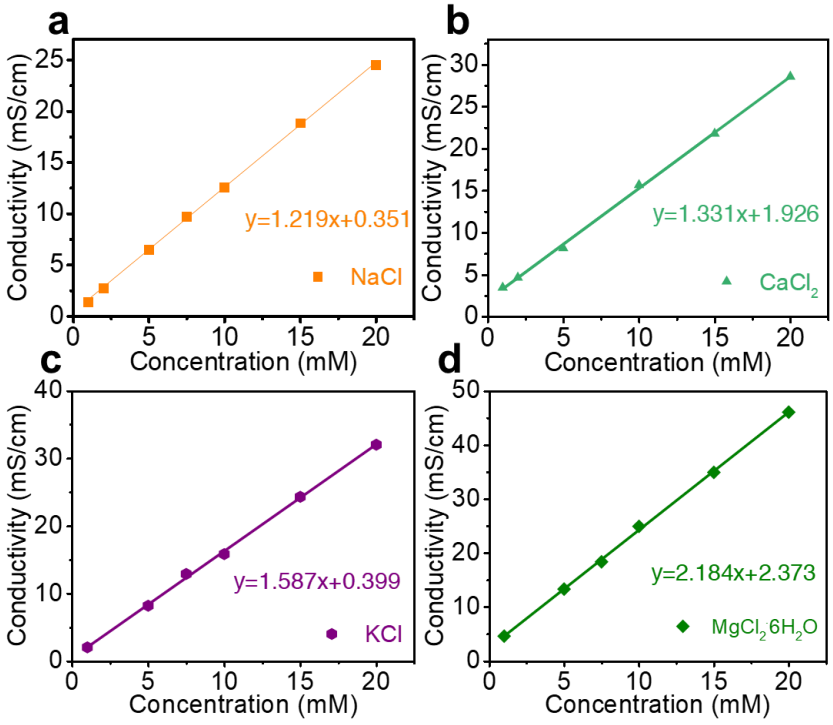

Figure S14 | The linear relationship between conductivity and concentration of various saline solutions. **a**, NaCl solution. **b**, $CaCl_2$ solution. **c**, KCl solution. **d**, $MgCl_2 \cdot 6H_2O$ solution.

Constant-voltage charge-discharge current density profile

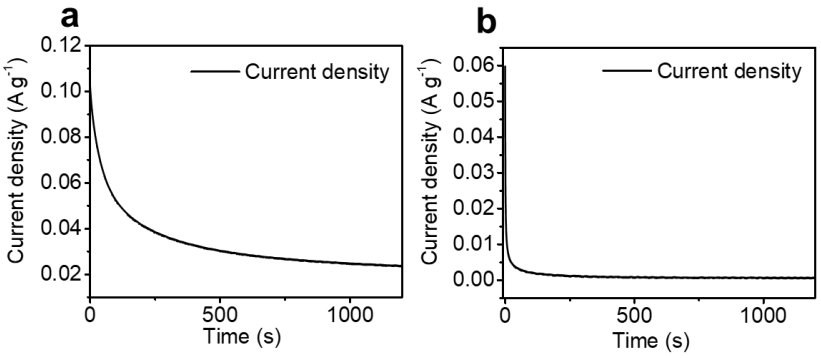

Figure S15 | a, Typical current density profiles of **a**, 1T′-MoS_2 and **b**, 2H-MoS_2 electrodes under single batch mode for NaCl solution.

XPS depth profile of MoS_2 electrode after CDI measurements

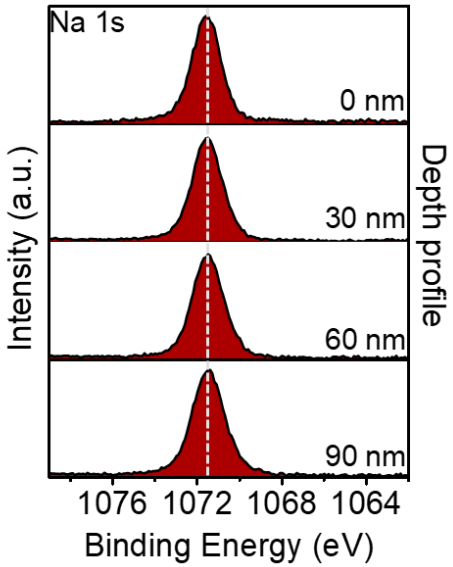

Figure S16 | Detailed spectra for the XPS depth profile of post measurements MoS_2 electrode with relative depth of 30, 60, 90 nm, showing the uniform distribution of Na element within MoS_2 channels of different thickness.

Post electro-sorption characterization of 1T'-MoS_2 electrode

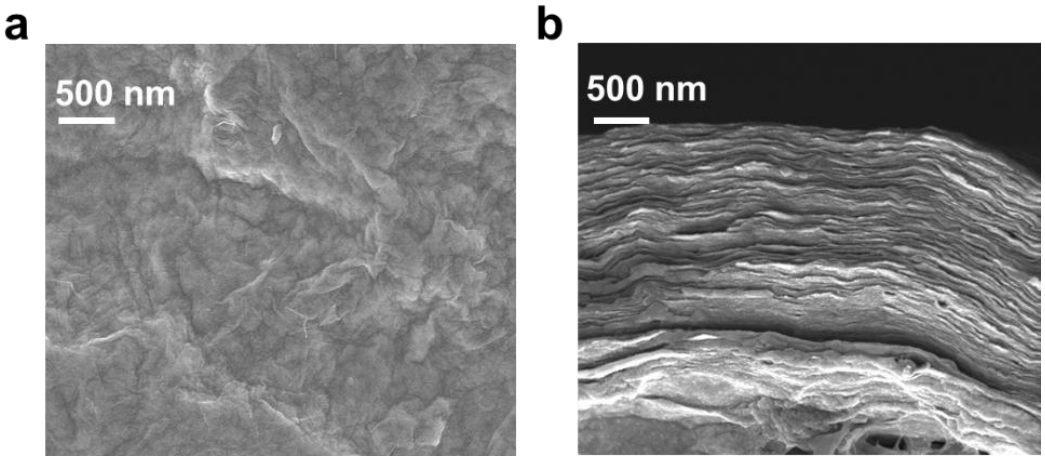

Figure S17 | a, Top-view and **b**, Cross-view of 1T′-MoS_2 electrode after electro-sorption cycling experiment. When comparing the morphology of electrode before (**Figure S7**) and after electro-sorption cycling experiment, no obvious changes can be observed, demonstrating the robust stability of our prepared electrodes.

Stability of 1T'-MoS_2 electrode before and after cycling repeats

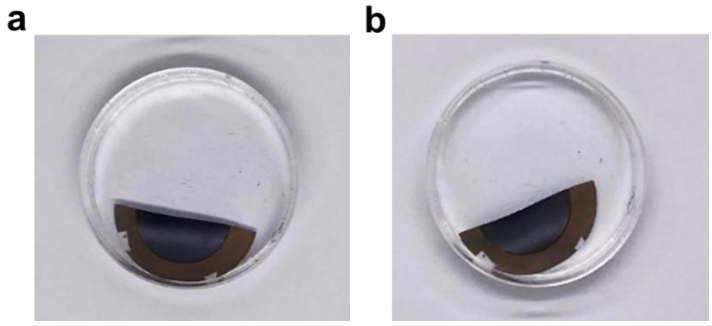

Figure S18 | Visual photos of electrodes immersed in saline solution before and after several repeats of testing, demonstrating the robust stability of our prepared electrodes. **a**: Starting photo, **b**: Photos after cycling performance.

Table S2 | Comparison of the CDI desalination performance of reported 2D-based and carbon-based electrodes for gravimetric and volumetric capacity

No.	Materials	Abbreviation	GAC_{NaCl} (mg/g)	VAC_{NaCl} (mg/cm^3)	References
1	MoS_2-graphene	MoS_2-G	19.4	14.3	[4]
2	Carbon aerogel	Gel-C	7	1.43	[5]
3	Hollow carbon sphere	h-C	2.3	0.64	[6]
4	Mesoporous carbon	Meso-C	14.7	3.56	[7]
5	Activated carbon	AC	11	6.26	[8]
6	Reduced GO/TiO_2	rGO/TiO_2	9.1	4.47	[9]
7	TiO_2/carbon	TiO_2/C	17.4	11.47	[10]
8	Carbon nanotube@MnO_2	CNT@ MnO_2	29.77	2.57	[11]
9	MnO_x nanofiber	MnO_x	27.8	1.87	[12]
10	MoS_2/carbon nanotube	MoS_2/CNT	10	18	[13]
11	Exfoliated MoS_2	Ex-MoS_2	8.81	16.51	[14]
12	1T′-MoS_2 nanolaminates	This work	**17.6**	**65.1**	This work

Initial adsorption sites in 1T'-MoS_2 and 2H-MoS_2 surface

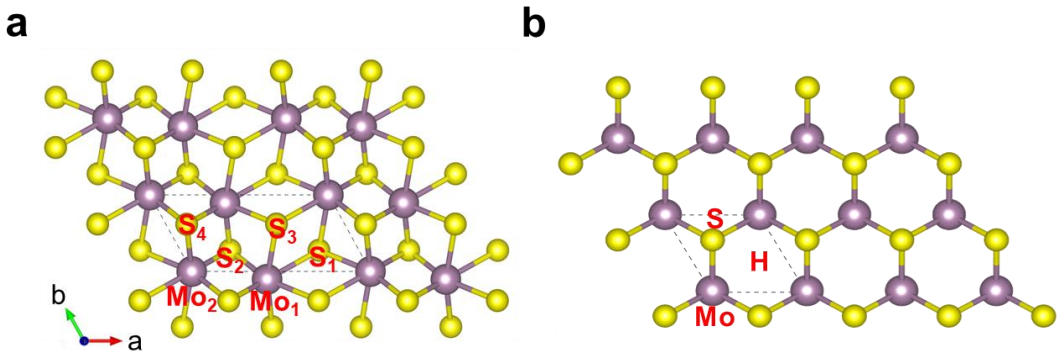

Site	E_{ad} (eV)	Site	E_{ad} (eV)
S_1	-2.380	Hollow	-0.706
S_2	-2.274	S	-0.447
S_3	-2.187	Mo	-0.726
S_4	-2.380		
Mo_1	-2.381		
Mo_2	-2.245		

Figure S19 | Atomic models illustrated initial adsorption sites on the surface of 1T′-MoS_2 (**a**) and 2H-MoS_2 (**b**). We discovered possible six sites and three sites for adsorption of potassium ions without the presence of water molecules, as depicted in **Figure a**, **b**. The adsorbed points are labelled as S_1, S_2, S_3, S_4, Mo_1 and Mo_2 in 1T′-MoS_2 while Mo, S and hollow(H) in 2H-MoS_2. Note that the K ions on the initial Mo_1 site would migrate to the bridge site between Mo_1 and S_1 for the 1T′-MoS_2. The attached table shows the specific adsorption values for different initial adsorption sites.

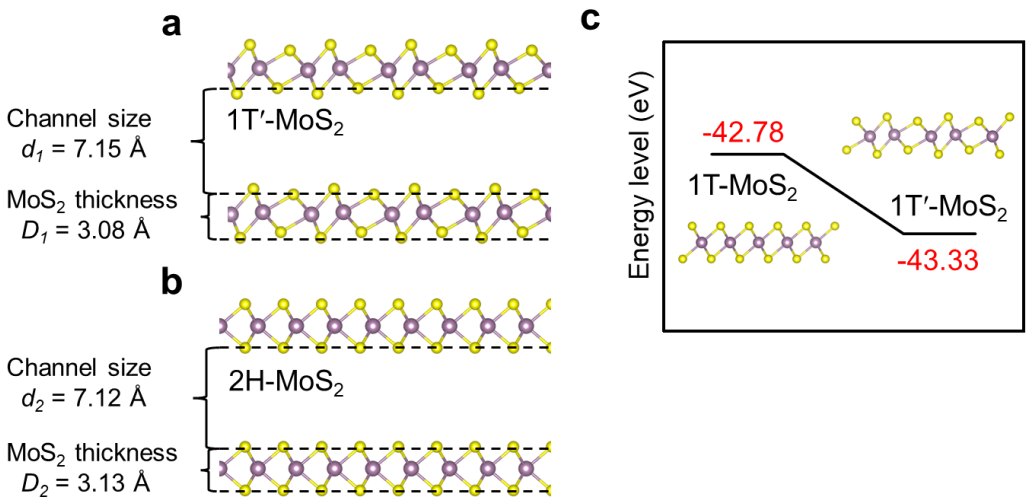

Figure S20 | Atomic model of 1T′-MoS_2, 2H-MoS_2 channels and phase stability of 1T and 1T′. **a**, Schematic illustration of 1T′-MoS_2 channels with channel size d_1 and MoS_2 thickness D_1. **b**, Schematic illustration of 2H-MoS_2 channels with channel size d_2 and MoS_2 thickness D_2. **c**, DFT calculation for the phase stability of 1T and 1T′ phases.

Site	E_{ad} (eV) Without water	E_{ad} (eV) With water	Site	E_{ad} (eV) Without water	E_{ad} (eV) With water
S_1	-2.785	-4.476	Hollow	-1.250	-2.924
S_2	-2.753	-4.434	S	-1.205	-2.908
S_3	-2.699	-4.475	Mo	-1.259	-2.927
S_4	-2.756	-4.431			
Mo_1	-2.793	-4.474			
Mo_2	-2.713	-4.476			

Table S3 | Ion-MoS_2 interaction for 1T′-MoS_2 and 2H-MoS_2 channels when potassium ion resides in different initial positions. The left columns show the adsorption energy between potassium ion and MoS_2 2D channels without solvent and the right ones with solvent. It is evident that the presence of water molecules significantly decreases the adsorption energy when comparing the left and right values.

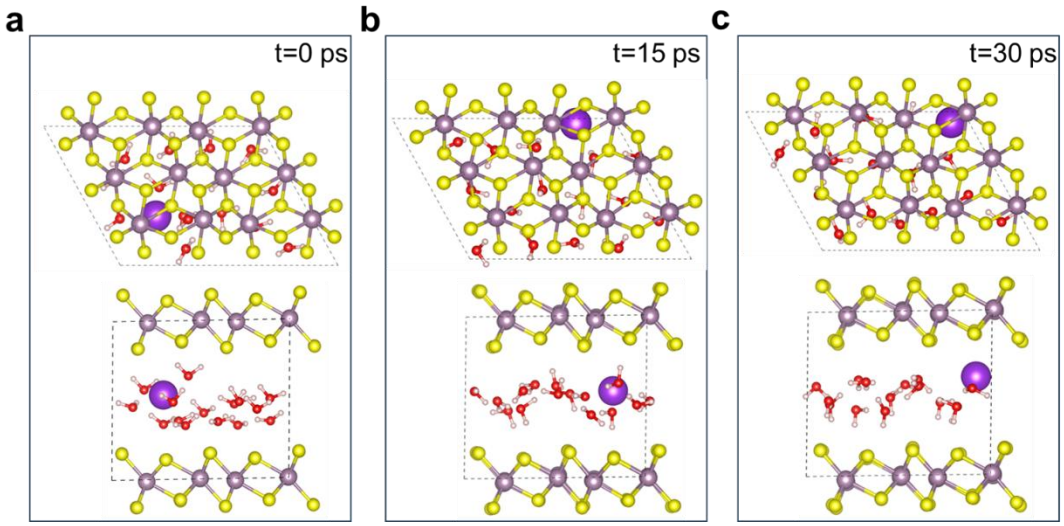

Figure S21 | Snapshots of a solvated potassium ion in 1T′-MoS_2 channel with respective time sequences of 0, 15, 30 ps.

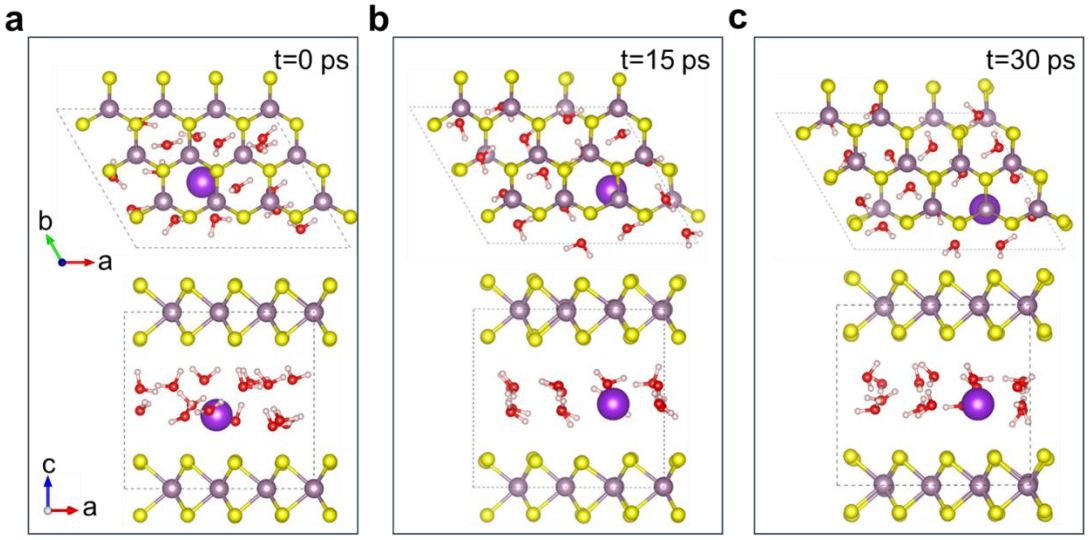

Figure S22 | Snapshots of a solvated potassium ion in 2H-MoS_2 channel with respective time sequences of 0, 15, 30 ps.

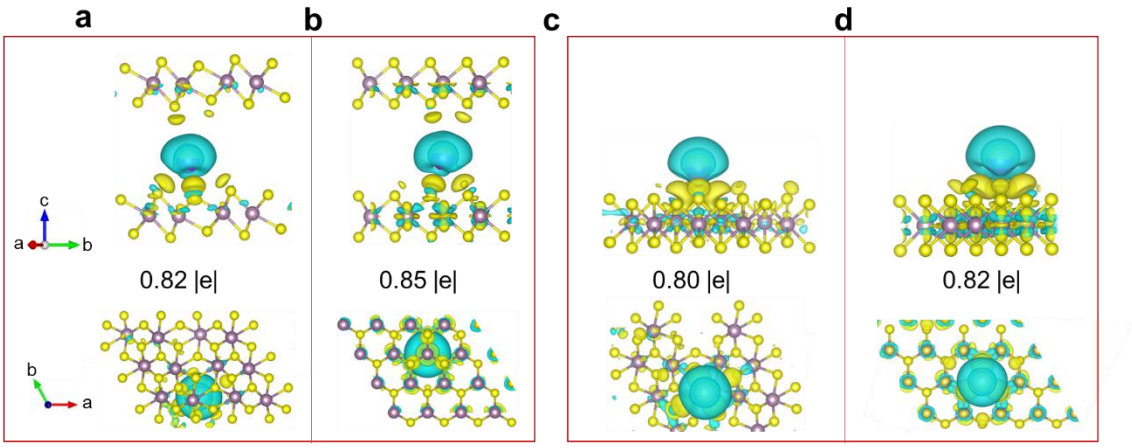

Figure S23 | Interfacial partial charge transfer for potassium ion in the 1T′-MoS_2 (**a**), 2H-MoS_2 (**b**) channels and on the vacuum surface of 1T′-MoS_2 (**c**), 2H-MoS_2 (**d**). The charge transfer increased from 0.80 |**e**| to 0.82 |**e**| when ions confined in the middle of channels. It indicated that channel effect is better for enhancement of partial charge transfer.

References

1. J. Kibsgaard; T.F. Jaramillo, Molybdenum Phosphosulfide: An Active, Acid-Stable, Earth-Abundant Catalyst for the Hydrogen Evolution Reaction. *Angew. Chem. Int. Ed.* **2014,** *53* (52), 14433-14437.
2. B. Dai; Y. Su; Y. Guo; C. Wu; Y. Xie, Recent Strategies for the Synthesis of Phase-Pure Ultrathin 1T/1T′ Transition Metal Dichalcogenide Nanosheets. *Chem. Rev.* **2024,** *124* (2), 420-454.
3. R. Yang; Y. Fan; L. Mei; H.S. Shin; D. Voiry; Q. Lu; J. Li; Z. Zeng, Synthesis of atomically thin sheets by the intercalation-based exfoliation of layered materials. *Nat. Synth.* **2023,** *2* (2), 101-118.
4. J. Han; T. Yan; J. Shen; L. Shi; J. Zhang; D. Zhang, Capacitive Deionization of Saline Water by Using MoS_2-Graphene Hybrid Electrodes with High Volumetric Adsorption Capacity. *Environ. Sci. Technol.* **2019,** *53* (21), 12668-12676.
5. H.-H. Jung; S.-W. Hwang; S.-H. Hyun; K.-H. Lee; G.-T. Kim, Capacitive Deionization Characteristics of Nanostructured Carbon Aerogel Electrodes Synthesized via Ambient Drying. *Desalination* **2007,** *216* (1), 377-385.
6. H. Wang; L. Shi; T. Yan; J. Zhang; Q. Zhong; D. Zhang, Design of Graphene-coated Hollow Mesoporous Carbon Spheres as High Performance Electrodes for Capacitive Deionization. *J. Mater. Chem. A* **2014,** *2* (13), 4739-4750.
7. R.T. Mayes; C. Tsouris; J.O. Kiggans Jr; S.M. Mahurin; D.W. DePaoli; S. Dai, Hierarchical Ordered Mesoporous Carbon from Phloroglucinol-glyoxal and its Application in Capacitive Deionization of brackish Water. *J. Mater. Chem.* **2010,** *20* (39), 8674-8678.
8. J.E. Dykstra; R. Zhao; P.M. Biesheuvel; A. van der Wal, Resistance Identification and Rational Process Design in Capacitive Deionization. *Water Res.* **2016,** *88*, 358-370.
9. A.G. El-Deen; J.-H. Choi; C.S. Kim; K.A. Khalil; A.A. Almajid; N.A.M. Barakat, TiO_2 Nanorod-intercalated Reduced Graphene Oxide as High Performance Electrode Material for Membrane Capacitive Deionization. *Desalination* **2015,** *361*, 53-64.
10. P. Srimuk; M. Zeiger; N. Jäckel; A. Tolosa; B. Krüner; S. Fleischmann; I. Grobelsek; M. Aslan; B. Shvartsev; M.E. Suss; V. Presser, Enhanced Performance Stability of Carbon/titania Hybrid Electrodes during Capacitive Deionization of Oxygen Saturated Saline Water. *Electrochim. Acta* **2017,** *224*, 314-328.
11. W. Shi; X. Zhou; J. Li; E.R. Meshot; A.D. Taylor; S. Hu; J.-H. Kim; M. Elimelech; D.L. Plata, High-Performance Capacitive Deionization via Manganese Oxide-Coated, Vertically Aligned Carbon Nanotubes. *Environ. Sci. Technol. Lett.* **2018,** *5* (11), 692-700.
12. B.W. Byles; D.A. Cullen; K.L. More; E. Pomerantseva, Tunnel Structured Manganese Oxide Nanowires as Redox Active Electrodes for hybrid Capacitive Deionization. *Nano Energy* **2018,** *44*, 476-488.
13. P. Srimuk; J. Lee; S. Fleischmann; S. Choudhury; N. Jäckel; M. Zeiger; C. Kim; M. Aslan; V. Presser, Faradaic Deionization of Brackish and Seawater via Pseudocapacitive Cation and Anion Intercalation into Few-layered Molybdenum Disulfide. *J. Mater. Chem. A* **2017,** *5* (30), 15640-15649.
14. F. Xing; T. Li; J. Li; H. Zhu; N. Wang; X. Cao, Chemically Exfoliated MoS_2 for Capacitive Deionization of Saline Water. *Nano Energy* **2017,** *31*, 590-595.